Stress and Frequency-dependent Properties of Poroelastic Anisotropic Rock

By
Sharif Munjur Morshed

A dissertation submitted to the Department of Earth and Atmospheric Sciences,

College of Natural Sciences and Mathematics

in partial fulfillment of the requirements for the degree of

Doctor of Philosophy

in Geophysics

Chair of Committee: Evgeny M Chesnokov

Committee Member: Aibing Li

Committee Member: Lorenzo Colli

Committee Member: Yasser M. Metwally

University of Houston
May 2021

Copyright 2021, Sharif Munjur Morshed

I dedicate this dissertation
to my father Abdul Matin, who's trust
always inspired me in difficult times. I am also
incredibly thankful to my wife, family, and friends.

Acknowledgments

I want to express my deepest gratitude to my supervisor Dr. Evgeny Chesnokov who inspired me with critical discussions and guidance and facilitated me from the beginning to the end of my doctoral study at the University of Houston. I would like to thank my committee members, Dr. Aibing Li, Dr. Lorenzo Colli, and Dr. Yasser Metwally, for their prudent questions, constructive suggestions, and the opportunity to present my dissertation.

I am very grateful to Dr. John Castagna, who was very supportive and helpful. A special thank goes to Lumina Geophysical, where I had an amazing work experience, and I learned reservoir geophysics a lot.

I can't appreciate enough Kefei Lu for his laboratory experiments and data. I am also indebted to Irina Bayuk and Alexandra Vikhoreva for support with the program code. I also like to take the opportunity to compliment my friends and colleagues Ismot Jahan, Avradip Ghosh, Yuandi Gan, Ramya Ravindranathan, Zhao Li, Ibrahim Albeshr, Lian Jiang, Morshad Ahmed, and many others.

Many thanks to the faculties and the staff of the Earth and Atmospheric Science Department of the University of Houston for providing me scholarships, financial supports, and a pleasant work environment.

Finally, I am very appreciative of the University of Houston.

Abstract

The poroelastic response of fluid saturated porous rock due to stress variations is of interest in geophysics and geomechanics as it has practical applications in reservoir depletion, fluid injection, time-lapse monitoring, and carbon dioxide sequestration. The effective stress in a poroelastic medium relates to applied pressure and pore pressure, with the Biot parameter (α) as a scaling factor of the pore pressure. This work offers an independent derivation of the tensor characteristics of α through elastic moduli, a microscopic effective medium derivation, and frequency-dependent behavior of α for an anisotropic medium. We derived simplified equations for isotropic rock subjected to confining pressure and pore pressure, isotropic rock under uniaxial stress considering the nonlinear part of elastic constants, and an equation of α for the frequency-dependent case. In the effective medium derivation, we assumed that the rock contains both isolated pores and connected pores saturated with liquid. We use the GSA method to Barnett shale core samples to link ultrasonic velocities with mineral composition and porosity data. We also use the GSA method in subsequent chapters to estimate the effective properties of a rock.

We corroborate our theoretical formulations by applying those equations to experimental data for different scenarios such as changes in confining pressure, pore pressure, and uniaxial stress. We calculated the Biot tensor for sandstone and shale. We found excellent agreement between theoretical prediction and experimental data. It is known that α varies significantly for changes in porosity and rock microstructure in isotropic rock. We also see as much as a 21% difference between horizontal and vertical components of α for transversely isotropic

(TI) rock for changes in uniaxial stress. We then estimated the frequency-dependent Biot tensor for TI models using numerical calculations. We noticed significant differences between vertical (α_{33}) and horizontal (α_{11}) components of α, especially at the surface seismic frequency band. However, uniaxial stress and horizontally aligned microstructure influence the elastic moduli and Biot tensor contrarily. In general, anisotropy due to uniaxial stress shows lower α_{33} and higher α_{11}. The anisotropy due to microstructure shows the opposite.

Table of Contents

List of Figures

List of Tables

Chapter 01

Introduction

1.1 Objective

The primary objective of this dissertation is to understand the behavior of poroelastic anisotropic rock for different stress scenarios and frequency-dependent cases to facilitate the analysis of elastic wave velocities for rock physics and reservoir geomechanical applications. The key factors that influence elastic wave velocities are the rock's internal microstructure, stress, and frequency of the measured data. The Biot coefficient (α) provides an important link between stress such as pressure, pore pressure, and uniaxial stress with elastic moduli, dependent on rock composition and pore texture. Therefore, we aimed at developing analytical equations of Biot tensor for different stress conditions incorporating the effective moduli in the equation for poroelastic and anisotropic rock. The effective moduli are obtained from the rock's microstructure data utilizing effective medium theory (EMT). We also aim to understand the effect of purely "stress-induced" anisotropy and microstructure related "inherent anisotropy" to the components of α tensor for transversely isotropic (TI) rock.

We also focus on dynamic cases as the frequency of different types of seismic data varies from ultrasonic frequency (~MHz) to surface seismic frequency (~Hz). We obtain an expression for frequency-dependent α to facilitate the evaluation of Biot α in terms of the measured data scale. The equations should improve rock deformation evaluation and compaction monitoring during reservoir depletion and fluid injection due to pore pressure change, reservoir engineering, and time-lapse monitoring.

1.2 Organization of the dissertation

Chapter 01 provides an overall organization of this dissertation and a brief description of the Barnett Shale data used in chapter 02 for effective medium investigation. Chapter two aimed at interpreting the microstructural properties from measured ultrasonic velocities of Barnett Shale data using the generalized singular approximation (GSA) method. It gives a brief derivation of the GSA method. It also explores the flexibility of the GSA method over other effective medium methods such as Eshelby (Eshelby, 1957), self-consistent approximations (SCA) (Willis, 1977), differential effective medium (DEM) (Nishizawa, 1980), and effective field method (Sevostianov and Kachanov, 2013). We model the effective stiffness tensor of rock matrix for 10 Barnett Shale core samples from the mineralogical composition data. Then, we invert velocity data to obtain porosity, pore aspect ratio, and pore connectivity parameter. The GSA method is used in chapter four to model the effective elastic properties of the rock matrix and solid grain.

Chapter three gives the detailed theoretical derivation of the Biot tensor (α_{ij}). First, we derive a static case general equation of Biot tensor (α_{ij}) for an anisotropic medium. We obtain analytical expressions for isotropic, cubic, hexagonal, and orthorhombic symmetry. We also receive an equation for isotropic rock subjected to confining pressure and pore pressure. We find another equation of Biot tensor for deviating part of the stress tensor, especially for uniaxial stress, considering the nonlinear part of elastic constants. Finally, we derive a macroscopic equation (i.e., the seismic waves' wavelength is higher than the size of the largest inhomogeneities) of α incorporating frequency for an anisotropic poroelastic medium, saturated with liquid of low viscosity. We use the GSA method in the static case and the Dyson equation's summation in the dynamic case employing Feynman's diagram technique. We show the expression for Biot parameter α in the general non-local situation when the Fourier transform of this parameter depends not only on the frequency but also on the wave vector.

Chapter 04 describes the application of theoretical equations to experimental data from the literature. We calculate the Biot tensor for changes in confining pressure, pore pressure, and uniaxial stress to different rock types such as sandstone and shale. We also describe why we choose particular types of data. We discuss the method we applied to get the results and associated issues and limitations. We examine our results to understand the "stress-induced" anisotropy and "intrinsic anisotropy" to the α tensor of transversely isotropic (TI) rock for the uniaxial stress case. We also estimate the frequency-dependent Biot tensor from four TI models using numerical calculations. In the numerical calculations, the background matrix is taken as isotropic. The inclusions are ellipsoidal in shape and saturated with gas and water. We use an algorithm utilizing the summation of Green's function based on n-point correlation approximation (Vikhorev and

Chesnonov, 2009). We provide the velocity and attenuation profiles for compressional wave, fast shear wave, and slow shear wave. Finally, we examine the results for the components of the Biot tensor.

Chapter 05 summarizes the overall contribution and findings of our research. It also describes the sources of errors, limitations, and suggestions for future work related to stress and frequency-dependent properties of anisotropic poroelastic rock.

1.3 Data: Barnett Shale

We use three sources of data for this dissertation. The first one is the Barnett Shale data measured at the University of Houston (Lu, 2016). The second source is the mineralogical composition and porosity data provided by Devon energy. The third type of data is collected from literature for poroelastic analysis purposes. A brief description of Barnett shale and related data are provided in the following paragraphs. We also describe additional details of data in the method and results section of each chapter.

The Barnett Formation is one of the successfully producing and major unconventional shale plays in the USA. It is a Mississippian age mudrock located in North Central Texas at the Fort Worth Basin (FWB). A subsurface stratigraphic section of the Bend Arch-Fort Worth basin from Pollastro et al. (2007) is provided in Figure 1.1, showing the total petroleum system (TPS) along with the Barnett Formation. The Barnett shale formation is found at depths usually from 6500-8500 ft below the surface in the core parts around the Dallas-Ft. Worth area of Tarrant county (Jarvie et al., 2007). It is thick, structurally deep, and interbedded with Forestburg Limestone Formation in the NE part of the FWB. The Barnett Shale occurs progressively at shallower depth towards the SW part of the basin. It thins out over the Chappel shelf formation in the west.

Even though Barnett Shale formation has been studied extensively for many different purposes, we didn't find any complete dataset of poroelastic measurements suitable with our theoretical equations. Nonetheless, poroelastic investigations proved to be very important as induced seismicity (Figure 1.2) within the FWB is often reported to be connected with pore-pressure change and poroelastic stress change (Quinones et al., 2019).

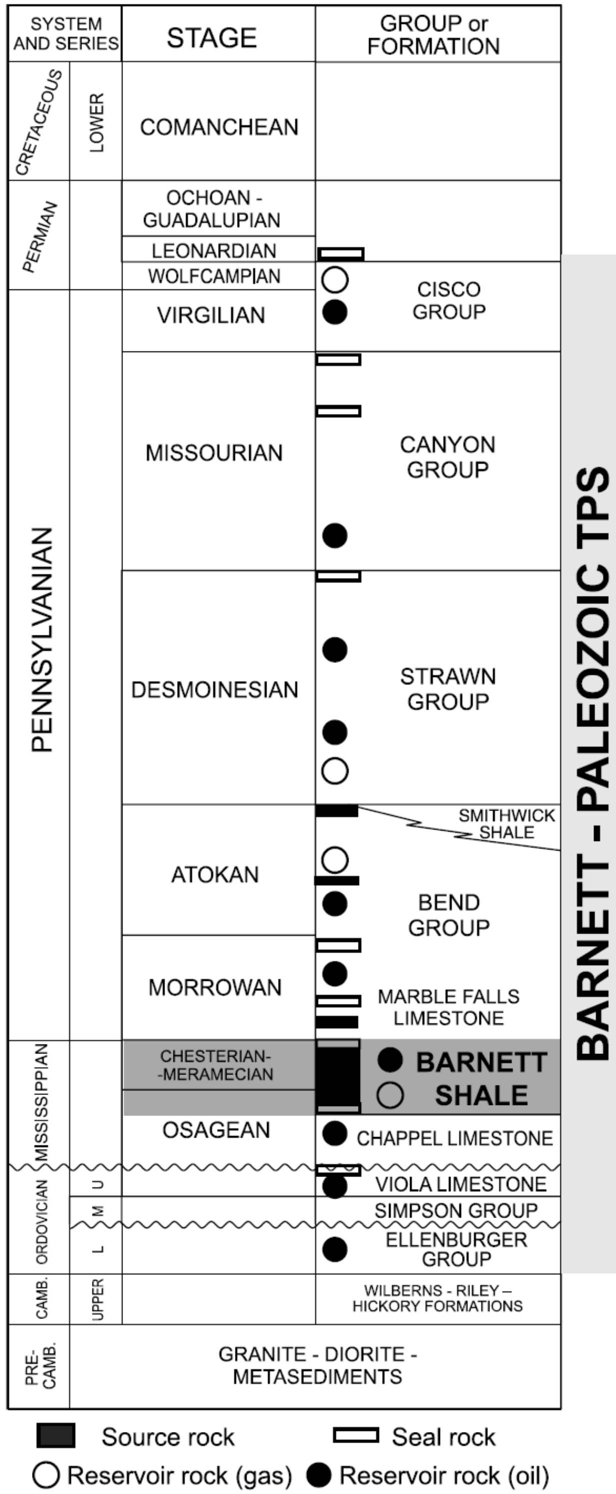

Figure 1.1: A generalized subsurface stratigraphic column of the Bend Arch- Fort Worth basin province showing the total petroleum system (TPS) with source rocks, reservoir rocks, and seal rocks (Pollastro et al., 2007).

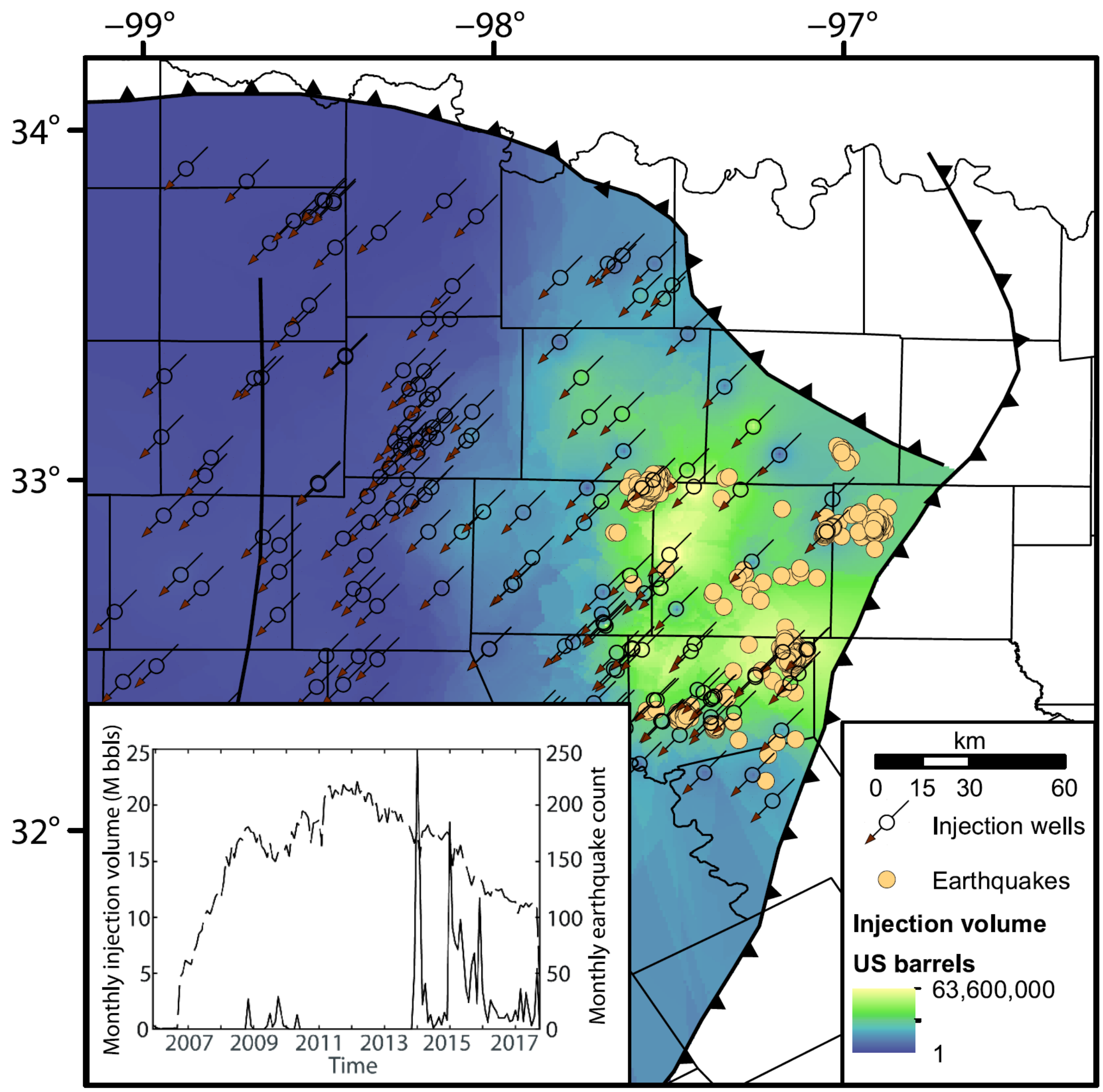

Figure 1.2: The map shows interpolated cumulative injection volumes into the Ellenburger formation underlying Barnett Shale formation. The circles and arrows represent earthquake and injection well locations, respectively. The figure is collected from Quinones et al. (2019).

Our Barnett Shale data came from the core samples provided by Devon Energy from six different wells (Table 1.1) of Fort Worth Basin in North Central Texas, USA. The samples are from Barnett Shale formation, and the depth of the samples ranges from 5105 ft to 7830 ft depending on the location of the well. The data consist of ultrasonic velocity, porosity, and mineralogical composition from the measurement and analysis of the core plugs.

Table 1.1: Description of the wells of the core sample data

No.	Well Name	Well No.	County	State	Depth (ft)	Sample No.
1	Adams Southwest	7	Wise	TX	6,586.00	A
2	Suger Tree	1	Parker	TX	5,105.00	C
3	Suger Tree	1H	Denton	TX	5,205.00	D
4	Jerome Russell	1H	Denton	TX	7,391.00	E
5	Jerome Russell	1	Johnson	TX	7,717.50	F
6	Rose Children Trust	1	Johnson	TX	7,630.00	G
7	Rose Children Trust	C-1	Tarrant	TX	7,830.00	H
8	Bonds Ranch	7	Wise	TX	7,180.00	J
9	Sol Carpenter Heirs	7	Wise	TX	7,590.00	K
10	Sol Carpenter Heirs	7	Wise	TX	7,391.00	L

The ultrasonic velocities were measured at the University of Houston (Lu 2016) with a three-plug technique (Figure 1.3) at atmospheric pressure and room temperature. This method allows obtaining phase velocities of compressional, fast shear, and slow shear waves at 0^o, $45^{o,}$ and 90^o angles from the vertical axis of a sample from three adjacent one-inch diameter plugs. The fast and slow shear waves propagating through the vertical plug have almost the same values for most of the samples (Table 1.2). Moreover, the slow shear waves of the horizontal plug have values close to the shear wave values of the vertical plug. Therefore, shear velocities of those samples represent to a good approximation VTI (Transversely isotropic with the vertical axis of symmetry) medium as the vertically polarized shear waves (Vsv) at 0° and 90° are equal for such medium.

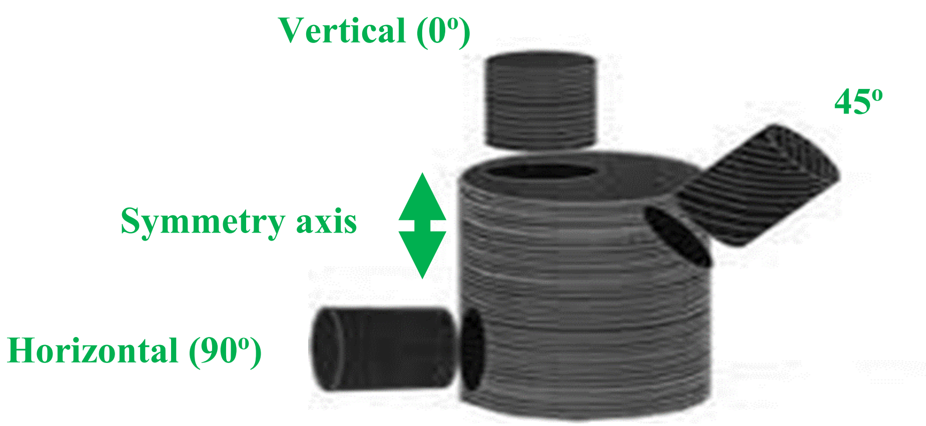

Figure 1.3: Traditional three-plug method for measuring ultrasonic velocities in transversely isotropic (TI) core samples. The symmetry axis is normal to the bedding planes. Three adjacent core plugs (one parallel, one perpendicular, and one 45° to the symmetry axis) were cut from the one core. The cartoon is adapted from Wang (2002).

It is very hard to control the cutting angle during the real measurement at 45° plug. However, the angle is very important for the accuracy of stiffness constant C13. Therefore, we provided the correct angle for 45° plug in Table 1.2 from Lu (2016).

The P-wave anisotropy coefficient (α_p) and shear wave anisotropy coefficient (α_s) (Chesnokov, 1977) of the measured data are shown in Figure 1.4. The coefficients mentioned above are more suitable for rocks with a high magnitude of anisotropy, such as Barnett Shale. The equations for the coefficients and their similarities with widely used Thomsen's notation (Thomsen, 1986) for weak anisotropy of a VTI media is provided in Appendix A. The ratio of the compressional wave velocity and fast shear wave velocity (Vp/Vs1) of the horizontal sample are plotted in Figure 1.5 with the averaged density of the three core plugs. Porosity data are also available from the three plugs for each depth point. However, the porosity values among the three plugs are not the same. Therefore, we use an averaged value to represent a sample. The mineralogical composition and porosity data is given in Chapter 02 as it helps understand the methods and results there.

Table 1.2: Velocities and densities of the core sample data

Sample No.	Degree	Vp(km/s)	Vs1(km/s)	Vs2(km/s)	Average Density (gm/cc)
A	90	4.923	2.983	2.339	
	0	3.130	2.324	2.334	2.535
	37.01	4.056	2.449	2.012	
C	90	4.701	2.861	2.227	
	0	3.015	2.144	2.126	2.403
	45.04	3.257	2.300	2.223	
D	90	4.965	2.905	2.303	
	0	3.630	2.230	2.230	2.504
	44.08	3.752	2.251	1.756	
E	90	4.690	2.949	2.305	
	0	4.477	2.815	2.793	2.663
	43.13	5.238	3.362	3.018	
F	90	4.897	3.047	2.853	
	0	3.565	2.368	2.368	2.746
	52.36	5.102	3.090	2.941	
G	90	4.469	2.905	2.083	
	0	2.944	2.313	2.313	2.511
	48.52	3.665	2.732	2.437	
H	90	4.734	3.014	2.249	
	0	3.160	2.176	2.176	2.564
	50.1	4.060	2.094	1.798	
J	90	4.928	3.149	2.589	
	0	3.810	2.313	2.313	2.529
	42.98	4.005	2.070	1.698	
K	90	4.784	3.027	2.407	
	0	3.053	2.320	2.308	2.431
	52.71	4.788	3.055	2.402	
L	90	5.301	3.125	2.810	
	0	3.787	2.533	2.520	2.700
	37.02	4.613	2.474	2.438	

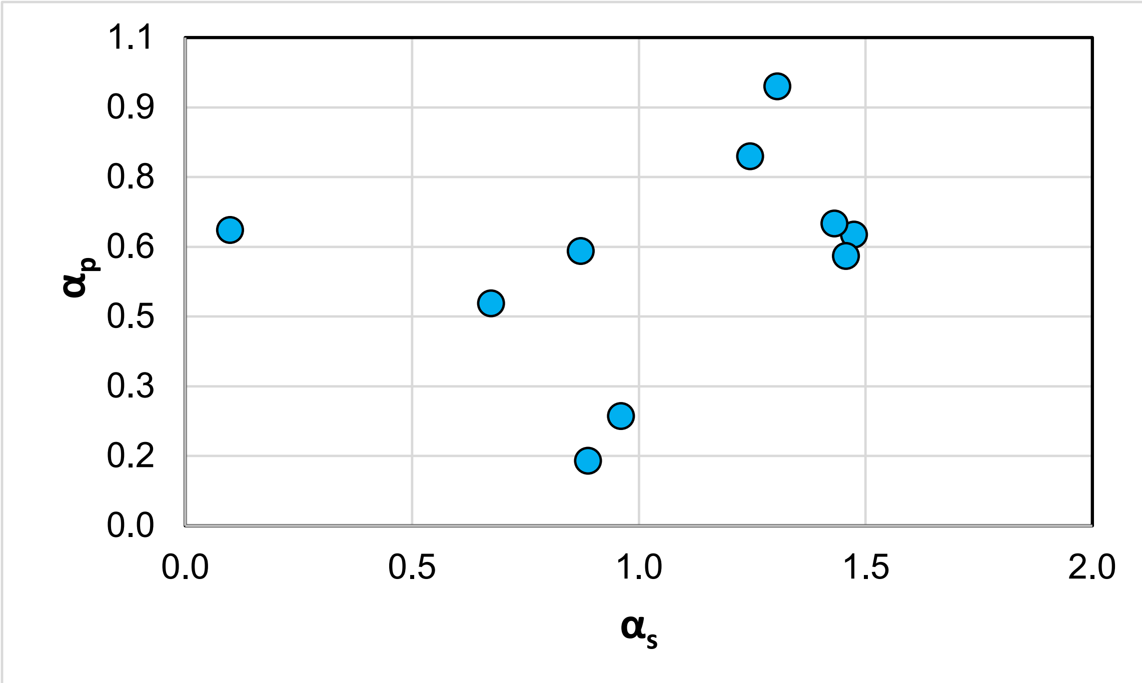

Figure 1.4: The P-wave anisotropy coefficient (α_p) and shear wave anisotropy coefficient (α_s) of the measured data are plotted.

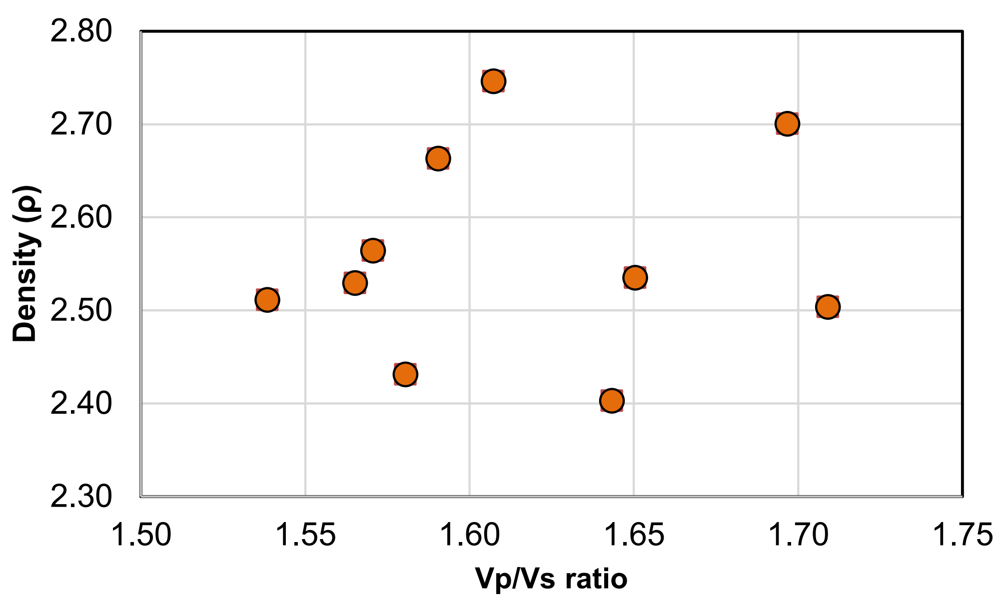

Figure 1.5: The ratio of the compressional wave velocity and fast shear wave velocity (Vp/Vs1) of the horizontal sample are plotted with the averaged density of the three core plugs.

Chapter 02

Effective Medium Theory: General Singular Approximation

2.1 Introduction

A part of this chapter is published in a peer-reviewed journal (Ghosh and Morshed, 2021). This chapter provides a brief theory of the generalized singular approximation (GSA) method (Bayuk and Chesnokov, 1998; Chesnokov et al., 2009), followed by GSA application to Barnett Shale core data. GSA is a mathematical approach of effective medium theory (EMT), which replaces an original heterogeneous rock volume with an equivalent homogeneous one called the effective media with the identical overall elastic properties of the original inhomogeneous and anisotropic media. In EMT, it is assumed that the seismic wavelength is much larger than the size of the rock heterogeneities.

The elastic properties of the rock are controlled by the microstructural properties such as mineralogical composition, pore and crack distribution, texture, and pore connectivity. Therefore, we established a connection between macroscopic properties and microstructural properties for ten core samples. We also use the GSA method in the following chapters for effective elastic properties of a rock for several circumstances.

2.2 Theoretical derivation of General Singular Approximation

The GSA effective medium method is based on comparing strain fields produced by two bodies of equal size and shape with the same boundary conditions (Bayuk and Chesnokov, 1998; Shermergor, 1977). One of the bodies is the original heterogeneous body, and the other one is a homogeneous comparison body. The stiffness tensor of both inclusion and matrix can be taken as anisotropic in GSA. A general formula of the GSA of the effective stiffness of a heterogeneous body with ellipsoidal inclusion is given as (Chesnokov et al., 2009):

$$\begin{aligned} C_{eff} &= \left\{ \sum_i \left(V_i C_i \int F_i(\chi_i;\varphi,\theta,\psi)[I - g_i(C_i - C^c)]^{-1} sin\theta d\chi_i d\theta d\varphi d\psi \right) \right\}^{-1} \\ &\times \left\{ \sum_i \left(V_i \int F_i(\chi_i;\varphi,\theta,\psi)[I - g_i(C_i - C^c)]^{-1} sin\theta d\chi_i d\theta d\varphi d\psi \right) \right\}^{-1} \end{aligned} \tag{2.1}$$

Where χ_i is the aspect ratio (AR) of the inclusion, I is the fourth rank unit tensor, C_i is the 4th rank stiffness tensor of the i-th component, V_i is the volume fraction of the i-th component, and C_c is the stiffness tensor of the comparison body. The tensor 'g' is the second derivative of the Green's function, and it depends on the properties of the comparison body and inclusion shape. $F_i(\chi_i;\varphi,\theta,\psi)$ is the orientation distribution function of the i-th component defined by the Euler angles. A detail description of orientation distribution function in GSA is available in Jiang (2013). Here, we provided a brief derivation of the GSA method is provided in Appendix B.

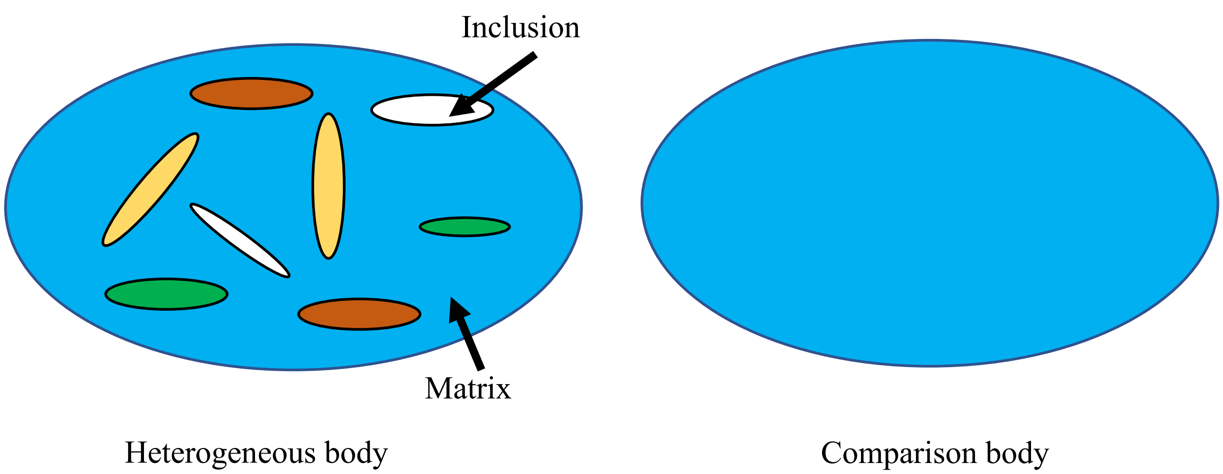

Figure 2.1: The left figure represents the original heterogeneous body with matrix and inclusions. The right figure is the assumed homogeneous comparison body.

The GSA method allows us to account for the degree of crack connectivity by the parameter f in the comparison body equation $C^C = C^m(1-f) + C^I f$, where C^m and C^I are, respectively, the elasticity tensors of mineral matrix and inclusions material. The f is an empirical parameter with values from 0 to 1. For a two-component matrix-inclusions media, the choice f =0 produces the upper Hashin-Shtrikman (HS) bound (Hashin and Shtrikman, 1963; Bayuk, Ammerman and Chesnokov, 2007). The upper HS bound represents a medium with isolated cracks in the mineral matrix. The other end (f =1) gives the lower HS bound. The lower HS bound corresponds to a medium where the ellipsoidal pieces of the matrix materials are surrounded by a connected phase of inclusions.

2.3 Comparison with other EMT methods

Currently, many EMT approaches exist, such as the self-consistent approximations (SCA) (Willis, 1977), differential effective medium (DEM) (Nishizawa, 1982), Hudson crack model (Hudson, 1980), Mori-Tanaka approach (Mori and Tanaka, 1973), and T-matrix approximation (Jakobsen, Hudson and Johansen, 2003). For the same rock model, all the EMT methods may produce similar results when the media is isotropic or porosity is small (i.e., total porosity less than 5% with crack porosity <0.06%) (Alkhimenkov and Bayuk, 2017). However, the Barnett Shale is not only heterogeneous in mineral composition but also contains several types of pores (Loucks et al., 2012), including low aspect ratio cracks. Some of the EMT approaches, such as DEM and SCA, do not account for the microstructure of the medium. Other methods, such as (Eshelby, 1957) and (Hudson, 1980), are limited to a small concentration of cracks. Therefore, we choose GSA as it allows a large volume of ellipsoidal pores with estimates of pores connectivity (through f parameter). The GSA method can be reduced to SCA and T-matrix approach using similar theoretical assumptions. Besides, the GSA method provides the best fit to the experimental data with known microstructure parameters (Bayuk and Chesnokov, 1998).

A comparison of effective elastic constants for different theoretical methods as a function of porosity is plotted in Figure 2.2 (Chesnokov E., personal communication, 2017). The considered model is an isotropic background medium with elliptical inclusions that are horizontally oriented.

Therefore, the effective medium has a TI (transversely isotropic) symmetry. The aspect ratio of the inclusions is 0.1. All the pores are inclusion pores (also known as crack-induced pores) in the models. Figure 2.2 demonstrates the flexibility of GSA over other methods as GSA can be used for stiff rocks where f values are low, as well as softer rocks where f values are high. We also made a comparison between the GSA and the effective field method (EF) (Sevostianov and Giraud, 2013) based on the same previous model. Our results are plotted in Figure 2.3. We found that EF method produces negative C33 and C13 at higher porosities. The reason is that the EF method is not supposed to be used at high porosity as it is limited to the "dilute concentrations" of inclusions, which is 1% porosity.

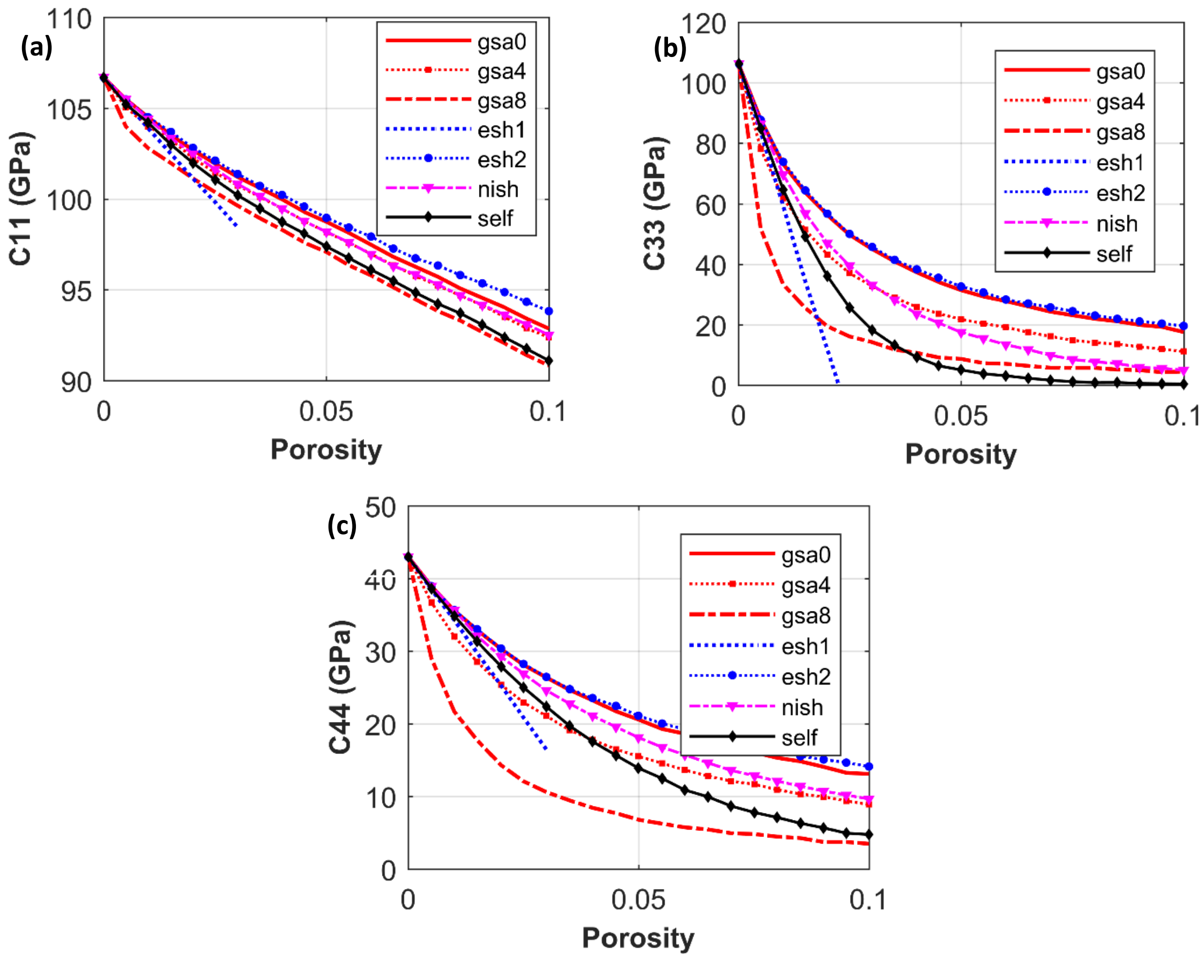

Figure 2.2: The components of effective elasticity matrix (**a**) C11, (**b**) C33 and (**c**) C44 with variations in porosity are plotted for different effective medium methods. The model contains horizontally aligned cracks in background isotropic medium (all minerals and clay are random and cracks are aligned). Notation: “gsa” is the GSA method, “esh1” is the Eshelby methods with constant strain at infinity, ‘esh2’ is the Eshelby method with constant stress at infinity, “nish” is the Nishizawa method, “self” is the self-consistent method. The digits after the “gsa” correspond to the connectivity parameter (f). The results are adopted from Bayuk and Chesnokov (1998).

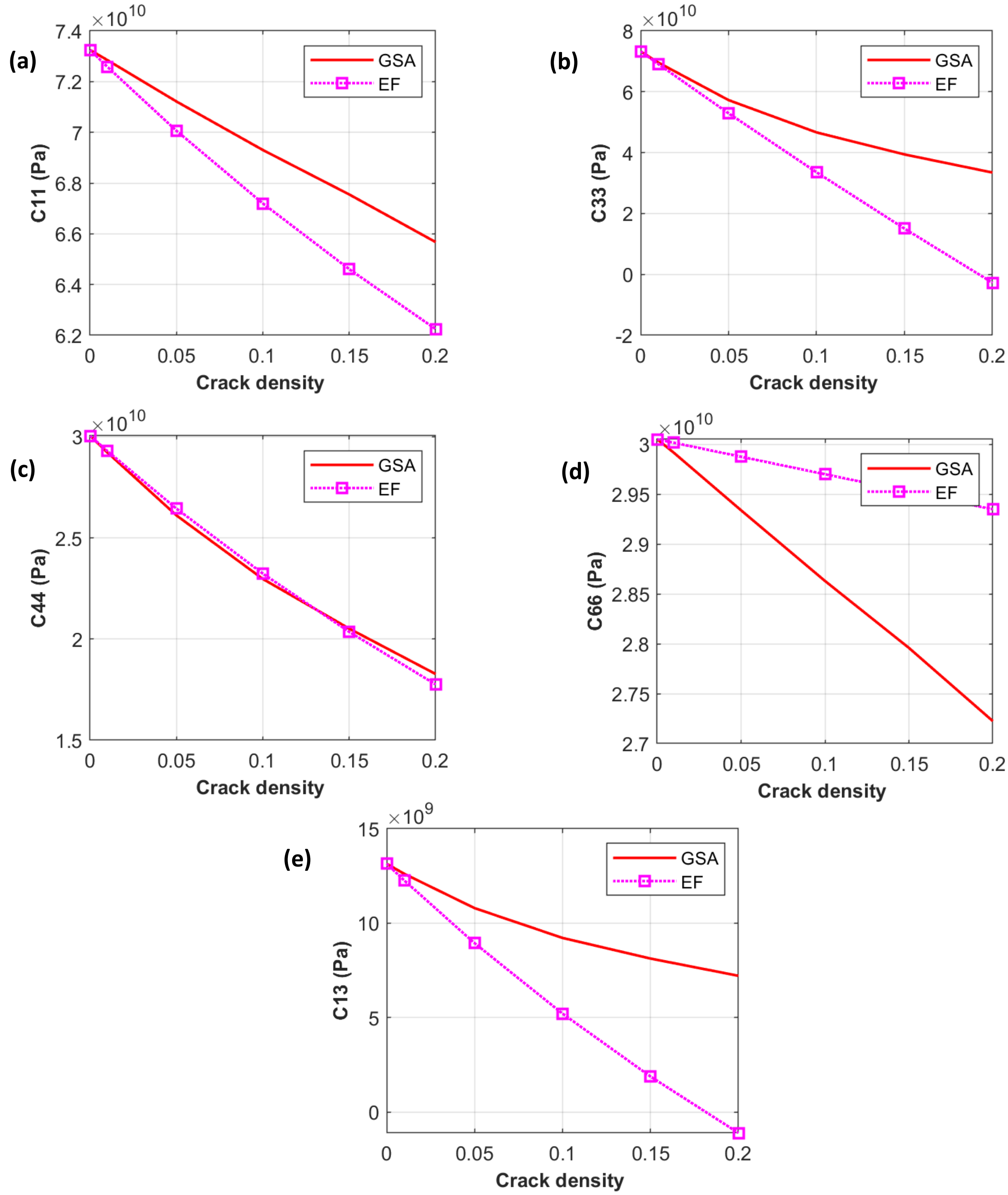

Figure 2.3: Effective elastic constants (**a**) C11, (**b**) C33, (**c**) C13, (**d**) C44 and (**e**) C55 at different crack densities for the case of horizontal ellipsoidal inclusion (aspect ratio =0.1). Legend notation: "gsa" is the GSA method, and "EF" is the Effective Field method.

2.4 Application to Barnett Shale data

2.4.1 Mineralogy and Lithofacies of Barnett Shale data

The Barnett Shale formation consists of several organic lithofacies, including siliceous mudstone, argillaceous lime mudstone, and argillaceous lime packstone (Loucks and Ruppel, 2007). The lithofacies vary substantially in mineral composition and pore types, depending on the depositional environment from proximal to distal areas of the delta. The XRD (X-ray diffraction) analysis (Table 2.1) of our core samples shows quartz-dominated lithofacies with less than 22% clay minerals (except Sample J). A ternary plot of the mineral composition data is also shown in Figure 2.4. The carbonate minerals are mostly calcite, which varies from 0 to 31 percent. The clay minerals generally range from 12 to 21 percent, where illite is the most abundant mineral. Some other minerals that are present in minor amounts are pyrite, halites, sulfates, and apatite.

The Barnett Shale is often described as siliceous mudstone as it lacks fissility, which is common in shale (Loucks and Ruppel, 2007). Some common types of pores in Barnett Shale are nanopores such as intraparticle pores, bedding parallel pores, and matrix pores (Loucks et al., 2009). So, nanopores form the gas's storage, and their main flow pathways are probably in bedding parallel direction. A detailed description of the mineralogy, porosity, and ultrasonic velocity is available on Lu (2016).

Table 2.1: Mineralogical compositions of the core samples from the XRD data

Sample No.		**A**	**C**	**D**	**E**	**F**	**G**	**H**	**J**	**K**	**L**
Quartz		**57**	**60**	**36**	**47**	**66**	**66**	**52**	**24**	**71**	**71**
Orthoclase		0	1	0	1	0	0	0	2	1	0
Albite		4	3	4	2	2	3	4	4	2	1
Pyrite		3	3	3	2	1	1	2	1	2	2
Total Carbonate		**12**	**13**	**31**	**20**	**7**	**5**	**13**	**15**	**4**	**7**
	Calcite	8	9	27	10	2	3	9	2	1	2
	Dolomite	2	1	2	7	4	0	3	8	1	1
	Aragonite	1	2	1	2	1	2	1	2	2	3
	Siderite	1	0	1	1	0	0	1	3	0	1
Sulfates & Halites		**5**	**5**	**13**	**7**	**2**	**4**	**6**	**10**	**2**	**1**
Apatite		1	1	1	1	0	0	1	0	1	1
Total Clay		**18**	**15**	**12**	**21**	**21**	**20**	**21**	**44**	**17**	**16**
	Smectite	2	2	2	4	3	2	3	12	2	2
	Illite	9	8	6	9	10	10	9	16	9	9
	Mixed Layer	4	3	2	4	4	4	4	14	3	3
	Kaolinite	1	1	1	1	1	1	2	0	1	1
	Mica	2	2	1	2	2	2	2	1	2	2
	Chlorite	0	0	0	1	1	0	1	1	0	0
Total		100	100	100	100	100	100	100	100	100	100

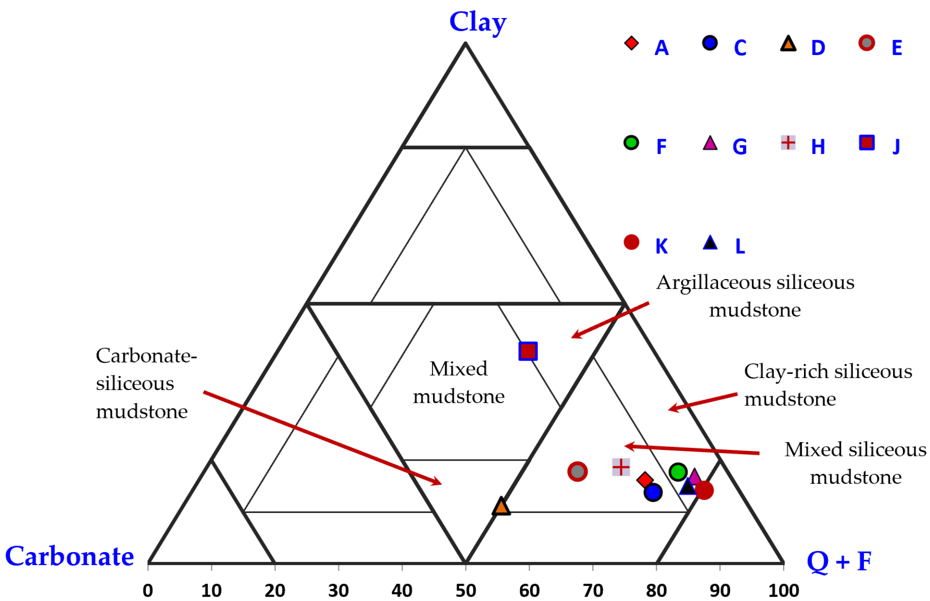

Figure 2.4: A ternary diagram of the Barnett Shale core samples, where Q+F are the quartz and feldspars. The mineral composition data was acquired using the X-ray diffraction (XRD) method. Most samples of the core data represent siliceous mudstone lithofacies.

2.4.2 Method and Results

The ultrasonic velocities of the core samples were measured using a three-plug method (Lu, 2016). A cartoon of ultrasonic measurements of a three-plug method is shown in Figure 1.2. For all our samples, the fast and slow shear waves in the vertical plug and horizontal plug's slow shear waves have almost equal values. Hence, we consider those samples as VTI (vertically transverse isotropic) medium. We applied the GSA method to establish a link between the rock microstructural properties and macroscopic elastic properties. Our approach is described in the following paragraph.

The Barnett Shale is composed of heterogeneous minerals (Table 2.1) and various types of pores (Loucks et al., 2012). Therefore, we apply the GSA scheme considering an anisotropic matrix containing both isolated and connected pores. We estimate the rock matrix's effective stiffness with Voigt-Reuss-Hill average, using volume fraction and elastic constants of minerals. The elastic constants and densities of minerals are collected from published literature (Ahrens and Johnson, 1995; Raymer, Tommasi and Kendall, 2000; Gebrande, 2005; Bayuk, Ammerman, and Chesnokov, 2007; Sanchez-Valle, Ghosh and Rosa, 2011; Jiang, 2013). Some minerals such as illite, kaolinite, and mica are known to cause intrinsic anisotropy of the rock. Therefore, we use an anisotropic stiffness tensor for those minerals. We consider illite and kaolinite as transversely isotropic and mica as monoclinic symmetry. We take elastic constants for smectite and mixed clay as isotropic. A list of the elastic constants and densities of clay minerals is provided in Table 2.2. We assume that the silt minerals such as quartz, albite, pyrite, calcite, dolomite, aragonite, siderite, halite, and apatite are isometric pieces of polycrystals having isotropic elastic moduli.

Table 2.2: Elastic constants and densities of clay minerals

Isotropic	**Bulk Modulus (GPa)**			**Shear Modulus (GPa)**		**Density (Kg/m^3)**
Smectite	7			3.9		2290
Mixed Clay	21.4			6.7		2600
Transversely Isotropic	C_{11} (GPa)	C_{13} (GPa)	C_{33} (GPa)	C_{44} (GPa)	C_{66} (GPa)	
Illite	179.9	14.5	55	11.7	70	2790
Kaolinite	171.5	27.1	5236	14.8	66.3	2520

We used two approaches to model the matrix stiffness. In general, we consider clay mineral as the matrix assuming clay minerals forms a connected domain, and silt minerals are inclusions. However, for some samples, the silt minerals are considered as a matrix if they constitute a significant percentage of the mineral composition, and the clay minerals are taken as inclusions. We present two thin sections of Barnett Shale lithofacies in Figure 2.5 to corroborate our approaches. One thin section (Figure 2.5(a), collected from Sone and Zoback, 2013) and a scanning electron microscope (SEM) image (Figure 2.5(b), from Metwally and Chesnokov, 2012) show that the silt minerals form a connected domain. However, the other thin section (Loucks and Ruppel, 2007) displays that the quartz and silt minerals are contained in a connected domain of clay matrix.

The connectivity parameter (f) is taken as zero for the estimation of matrix stiffness. Thus, we received the stiffness tensor of the solid matrix in the first step. In the second step, we invert the lab measured velocities and densities utilizing a simulated annealing algorithm to estimate the unknown data such as pore aspect ratio, porosity, and the connectivity (f) parameter. We use calculated matrix stiffness during inversion.

The quasi-phase velocities of Vp, Vs_1, and Vs_2 from the GSA inversion are plotted with the experimental data in Figure 2.6. The GSA results are a good fit with the measured velocities. The GSA velocities and measured velocities are in better agreement at 0^o and 90^o angle of incidences, which is reasonable because the data quality is better at those angles. Elastic wave velocity measurements of 45^o degree plugs are usually challenging and prone to error (Lu, 2016). The inverted microstructural data is given in Table 2.3. The f (i.e., connectivity parameter) values for the most samples are 0.9, which implies most of the cracks are connected. The higher values of the average aspect ratio (e.g., 0.45) indicates pores are subspherical to ellipsoidal. The difference between the elastic constants of the GSA modeled data and lab measured data of five elastic constants are shown in Figure 2.7. The errors (i.e. difference) are highest for C13 and lowest for C33.

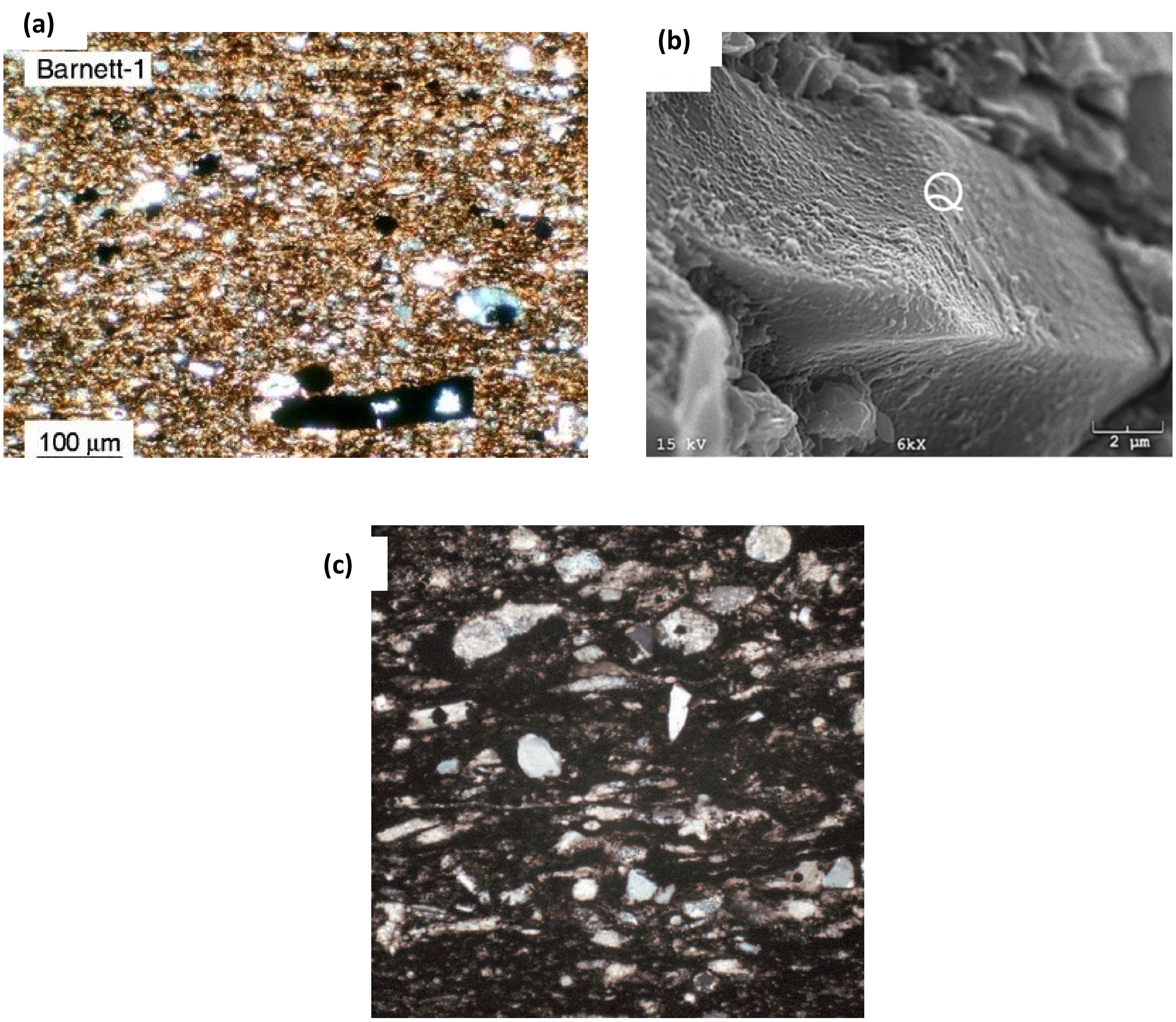

Figure 2.5: (a) A thin section image of Barnett Shale showing silt minerals formed a connected phase (Sone and Zoback, 2013), (b) an SEM image showing detrital quartz in Barnett Shale (Metwally and Chesnokov, 2012), (c) a thin section image shows fine-grained quartz and skeletal debris in a thin lamina of siliceous mudstone (Loucks and Ruppel, 2007).

To summarize, GSA provides a good correlation between microstructure properties and elastic properties, including stiffness tensor, velocities, and porosities from low to high concentration of inclusion (e.g., cracks). The sources of error in this study can be experimental error and methodology error. As data were measured from three core plugs to represent one media, we also accept that the mineral composition, microstructure, and porosities are sometimes not exactly the same among the three plugs.

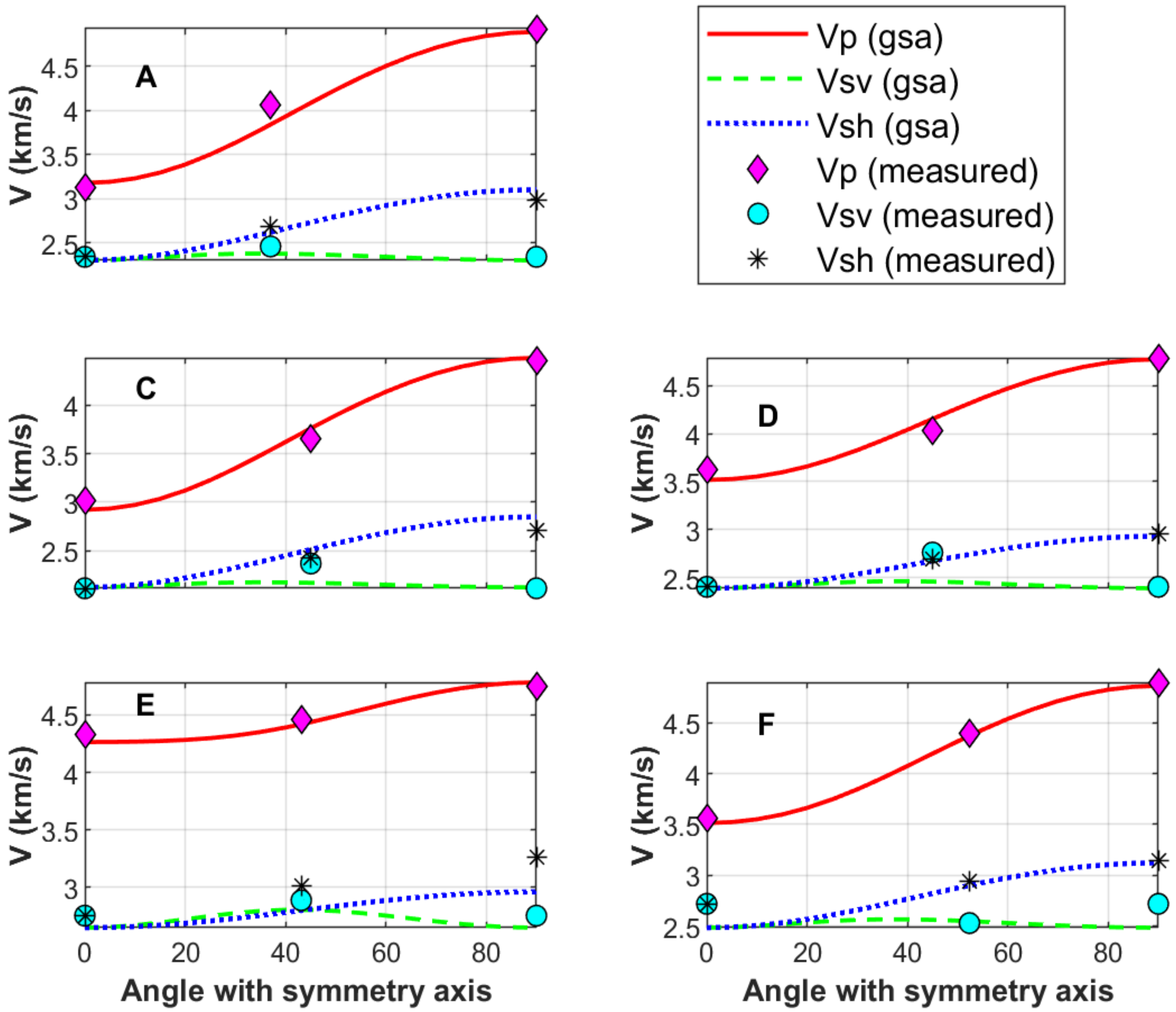

Figure 2.6: The quasi-phase velocities from the GSA method are plotted along with lab measured velocities as a function of angle from the vertical axis of symmetry (assuming VTI media) for all ten samples. The sample number is labeled on the upper left part of each plot. The legend represents Vp, Vsh, and Vsv as compressional, horizontally polarized shear, and vertically polarized shear wave velocity, respectively.

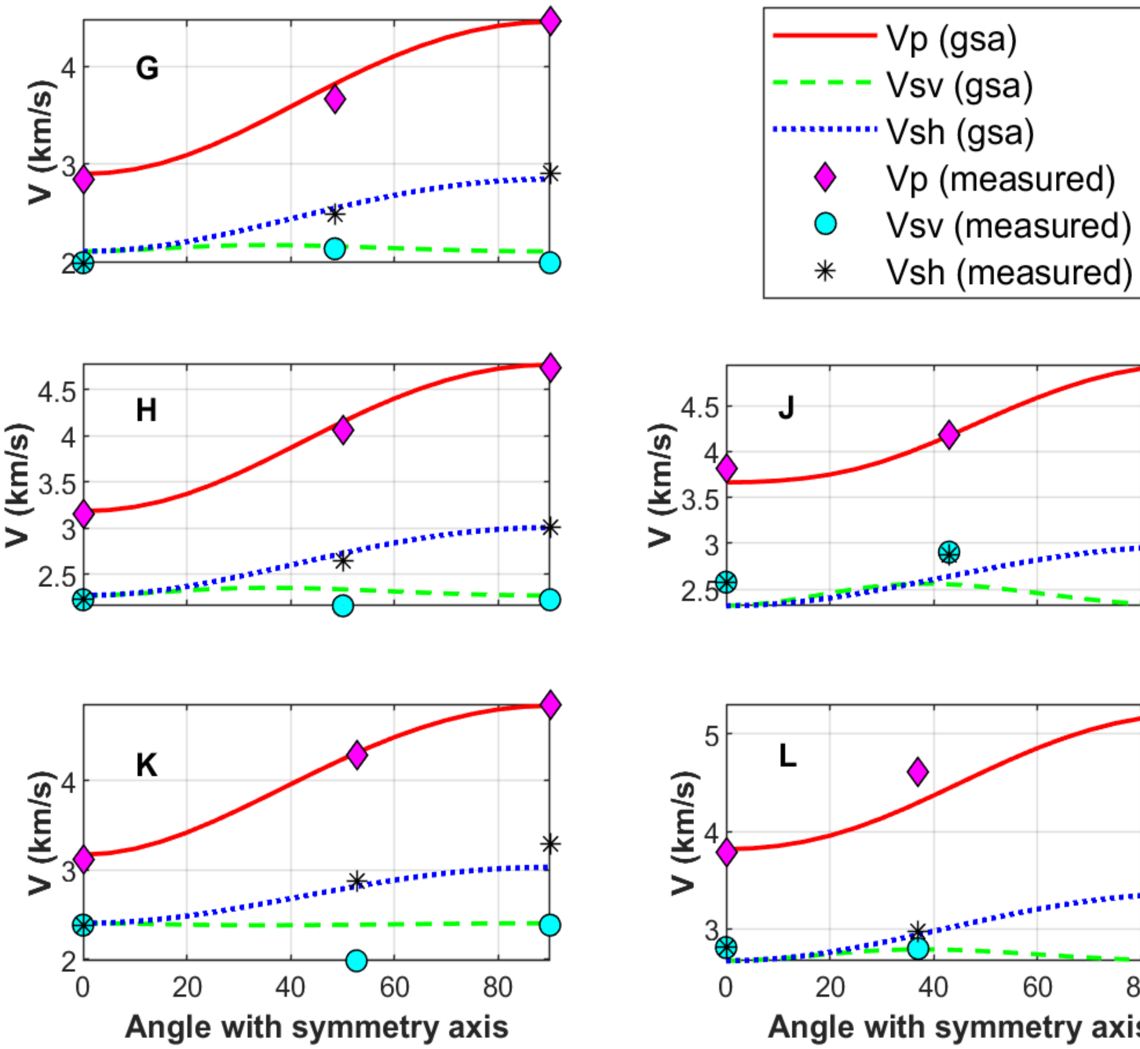

Figure 2.6: (continued) The quasi-phase velocities from the GSA method are plotted along with lab measured velocities as a function of angle from the vertical axis of symmetry (assuming VTI media) for all ten samples. The sample number is labeled on the upper left part of each plot. The legend represents Vp, Vsh, and Vsv as compressional, horizontally polarized shear, and vertically polarized shear wave velocity, respectively.

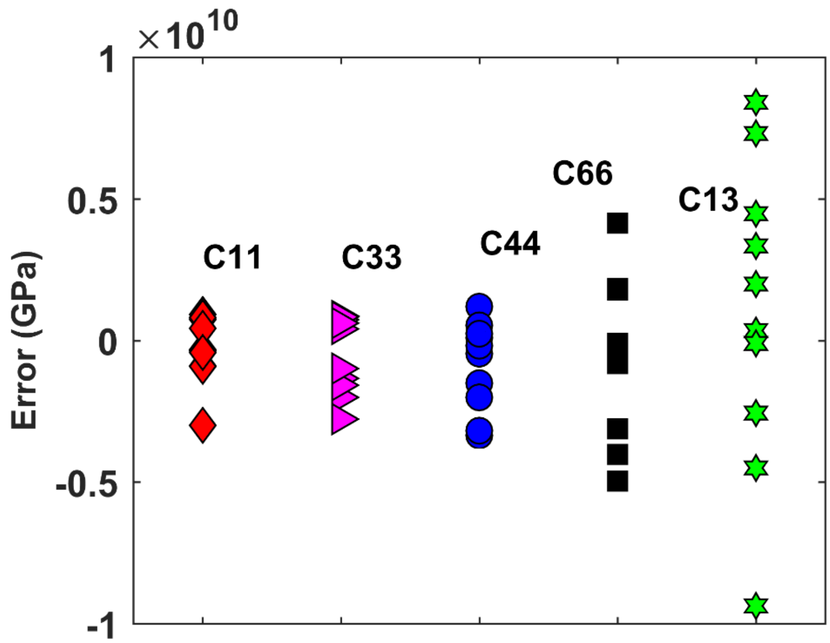

Figure 2.7: The error plot (i.e. difference between modelled data and measured data) of five elastic constants. The errors are highest for C13 (obtained using 45° sample) and lowest for C33.

Table 2.3: Inverted microstructural data with measured porosity data

Shale Cores	Connectivity (f)	Porosity (GSA)	Aspect ratio (GSA)	Porosity (cal)
A	0.900	5.00%	0.4510	7.35%
C	0.900	9.00%	0.5010	10.70%
D	0.800	11.10%	0.5010	8.2%
E	0.800	7.01%	0.9510	7.6%
F	0.900	5.01%	0.5010	3.80%
G	0.900	8.00%	0.5010	6.10%
H	0.800	12.01%	0.4510	9.10%
J	0.500	3.00%	0.3010	0.04%
K	0.900	6.01%	0.5010	6.88%
L	0.900	2.01%	0.5000	0.10%

Chapter 03

Theory: Biot effective stress parameter in poroelastic anisotropic media

3.1 Introduction

A part of this chapter is published in the Geophysical Prospecting journal (Morshed, Chesnokov and Vikhoreva, 2021). This chapter provides an independent derivation of the tensor characteristics of Biot effective stress parameter (α) through elastic moduli, a microscopic effective medium derivation, and frequency-dependent behavior of α for an anisotropic medium. We provide equations for the following cases -

1. A basic equation for Biot tensor (α_{ij}) in the general case of an anisotropic medium under stress, and analytical expressions for the primary and commonly used types of symmetry in geophysics, such as isotropic, cubic, hexagonal, and orthorhombic symmetry.
2. A general equation for the influence of stress on the Biot tensor (α_{ij}), and a simplified equation for isotropic rock subjected to confining pressure and pore pressure.
3. An equation for the Biot tensor in terms of deviating part of the stress tensor, especially for uniaxial stress considering the nonlinear part of elastic constants.
4. An equation of α_{ij} for the frequency-dependent case.

The poroelastic response of fluid saturated porous rock due to stress variations is of interest in geophysics and geomechanics as it has practical applications in reservoir characterization, time-lapse monitoring, fluid-induced seismicity, and hydraulic fracturing. The effective stress, which is the core of poroelastic theory, is a combined effect of the externally applied stress and the internal pore pressure. Terzaghi (1923) first introduced the concept of effective stress in two extreme cases of high and low porosity. However, much of the theoretical framework of poroelasticity for rocks with random porosity was built in the classical Biot papers (Biot and Willis, 1957; Biot, 1962), which shows that the Biot-Willis effective stress coefficient (α), which ranges from 0 to 1, controls effective stress. Many workers have studied the effective stress behaviour and Biot coefficient (α), both in theory (Nur and Byerlee, 1971; Zimmerman, 1991; Berryman, 1992; Cheng, 1997; Gurevich, 2004) and with experimental investigations (Skempton, 1954; Todd and Simmons, 1972; Siggins and Dewhurst, 2003; Zhou and Ghassemi, 2019; Ma and Zoback, 2017). Based on phenomenological considerations, Nur and Byerlee (1971) expressed α for isotropic media in terms of the effective elastic moduli of a medium with empty pores. A decent review of α for isotropic media is also presented in Gurevich (2004). The values of α are measured in core samples for different types of isotropic rocks, and usually, it varies from 0.49 to 0.79 (Siggins et al., 2004).

Several authors such as Carrol (1979), Thompson and Willis (1991), and Cheng (1997) theoretically formulated α as a second rank tensor for an anisotropic rock using different approaches. Even though Carrol's phenomenological derivation was reasonably criticized by Thompson and Willis (1991), its results turned out to be absolutely correct. It has been proven by the authors (Chesnokov et al., 1995; Bayuk and Chesnokov, 1998) based on a microscopic derivation of the Biot-Willis tensor parameter. In this work, we adopt the microscopic derivation of α with theoretical expression for stress and frequency dependency. In the effective medium derivation, we assumed that the rock contained both isolated pores and connected pores saturated with liquid. We also focus on the theoretical formula of the Biot tensor to easily apply it to the experimental data in terms of applied pressure and pore pressure. We include the nonlinear elastic tensor with a regular second-order elastic tensor for the case of applied uniaxial stress.

Anisotropy in seismic waves is related to both rock microstructure and the stress state, which is other than isotropic. Anisotropy caused by nonisotropic or deviatoric stress is often termed induced anisotropy (Nur and Simmons, 1969; Nikitin and Chesnokov, 1981; Rasolofosaon, 1998; Sayers, 2010). Anisotropy caused by microstructure is known as intrinsic or inherent anisotropy. Therefore, defining the Biot tensor in terms of elastic moduli enables us to link it to seismic wave velocities, rock microstructure, and subsurface stress. Variations in seismic wave velocities caused by the reservoir stress changes play a significant role in reservoir compaction and time-lapse monitoring of stress field analysis (Sayers, 2010; Herwanger and Koutsabeloulis, 2011). The Biot α is particularly crucial in compaction monitoring as it measures the susceptibility to deformation of the reservoir rock due to pore pressure.

The elastic wave velocities that we use for exploration seismology often vary in terms of scale from ultrasonic frequency (~MHz) to surface seismic frequency (~30Hz) as they sample varied amounts of rock volume (from a few centimeters to a couple hundreds of meters). We obtain an expression of α incorporating frequency to facilitate the evaluation of Biot α in terms of the scale of the measured data. We write a microscopic equation of motion for a very small volume of an anisotropic poroelastic medium saturated with a fluid of low viscosity. Then, we find the macroscopic equation (i.e., the wavelength of seismic waves is much higher than the size of the largest inhomogeneities). We use the singular approximation method in the static case, and the summation of the Dyson equation in the dynamic case utilising the Feynman's diagram technique (Chesnokov et al., 1995). We show the expression for Biot parameter α in the general non-local situation when the Fourier transform of this parameter depends not only on the frequency but also on the wave vector.

3.2 Basic equations and derivation of the Biot tensor (α_{ij})

The phenomenological theory of poroelasticity was established by Biot (Biot, 1956; Biot and Willis, 1957; Biot, 1962) for a fluid-saturated rock with connected pores. According to Biot and Terzaghi's (Terzaghi, 1923) notion, the averaged elastic deformation (ε_{ij}) is an additive function of the averaged stress (σ_{ij}) and pore pressure (P). Therefore, total strain is related to the effective stress (σ_{kl}^{eff}). Let us write a constitutive equation for the effective stress of a dry medium as below

$$\varepsilon_{ij}^{eff} = S_{ijkl}\sigma_{kl}^{eff} \tag{3.1}$$

Here S_{ijkl} is the compliance of a medium containing both isolated pores and connected pores.

In the general case of an anisotropic poroelastic medium, the effective stress is linked with the confining stress and pore pressure by the following formula

$$\sigma_{ij}^{eff} = \sigma_{ij} - \alpha_{ij}P \tag{3.2}$$

where α_{ij} is the 2nd rank Biot tensor.

To derive the expression for the Biot tensor through elastic modulus of the porous media in the general anisotropic case, we will follow the work of Nur and Byerlee (1971). For this purpose, let us separate the stress tensor in two parts

$$\sigma_{ij} = \sigma_{ij}^{(1)} + \sigma_{ij}^{(2)}$$

where $\sigma_{ij}^{(1)}$ is the differential stress and equal to $(\sigma_{ij} - P\delta_{ij})$, and $\sigma_{ij}^{(2)}$ is identically equal to $P\delta_{ij}$.

Due to its additivity, the deformation tensor (ε_{ij}) also divided into two parts, such as

$$\varepsilon_{ij}^{eff} = \varepsilon_{ij}^{1} + \varepsilon_{ij}^{2} \tag{3.3}$$

where ε_{ij}^{2} is the deformation caused by the pore pressure of the liquid.

$$\varepsilon_{ij}^{2} = S_{ijkl}^{o} P\delta_{kl} \tag{3.4}$$

Here S_{ijkl}^{0} is the compliance tensor of the skeleton material, and P is the pore pressure. The first term (ε_{ij}^{1}) describes deformation due to the stress differences between the pore pressure and the stress tensor.

$$\varepsilon_{ij}^{1} = S_{ijkl}\left\{\sigma_{kl} - P\delta_{kl}\right\} \tag{3.5}$$

By using formulas (3.1) to (3.5) and substituting into (3.3), we obtain

$$S_{ijkl}\sigma_{kl}^{eff} = S_{ijkl}\sigma_{kl} - \left\{S_{ijkl} - S_{ijkl}^{o}\right\} P\delta_{kl} \tag{3.6}$$

Multiplying (3.6) by the tensor of elasticity C_{ijkl} for a poroelastic medium with empty pores, we will obtain expressions for the effective stress tensor

$$\sigma_{ij}^{eff} = \sigma_{ij} - \left\{ I_{ijkl} - C_{ijpq} S_{pqkl}^{o} \right\} P \delta_{kl} \tag{3.7}$$

By comparing equation (3.2) and (3.7), we obtain the expressions for the Biot tensor as

$$\alpha_{ij} = \delta_{ij} - C_{ijkl} S_{klmm}^{o} \tag{3.8}$$

where δ_{ij} is the Kronecker delta tensor.

The formulae (3.8) allow us to obtain the expressions α_{ij} for different types of symmetry. We provide below explicit expressions for the most useable types of symmetries in geophysics.

Isotropic symmetry

In this case, tensors C_{ijkl} and S_{klmn}^{o} can be presented in a form (Shermergor, 1977)

$$C_{ijpq} = K\,\delta_{ij}\delta_{pq} + \mu\left(\delta_{ip}\delta_{jq} + \delta_{iq}\delta_{jp} - \frac{2}{3}\delta_{ij}\delta_{pq} \right) \tag{3.9}$$

$$S_{pqmn}^{o} = \frac{1}{9K^{o}}\delta_{pq}\delta_{mn} + \frac{1}{4\mu^{o}}\left(\delta_{pm}\delta_{qn} + \delta_{qm}\delta_{pn} - \frac{2}{3}\delta_{pq}\delta_{mn} \right) \tag{3.10}$$

where K and μ are the bulk modulus and shear modulus of the porous rock. K^{o} and μ^{o} are the bulk modulus and shear modulus of the skeleton material. When m=n, the equation (3.10) takes the form

$$S^o_{pqmm} = \frac{1}{3K^o}\delta_{pq} + \frac{1}{4\mu^o}\left(2\delta_{pq} - 2\delta_{pq}\right) = \frac{1}{3K^o}\delta_{pq} \tag{3.11}$$

Substituting expressions (3.9) and (3.11) in to (3.8), leads to formulae:

$$\alpha_{ij} = \delta_{ij} - \left[K\delta_{ij}\delta_{pq} + \mu\left(\delta_{ip}\delta_{jq} + \delta_{iq}\delta_{jp} - \frac{2}{3}\delta_{ij}\delta_{pq}\right)\right]\frac{1}{3K^o}\delta_{pq}$$

$$= \delta_{ij} - \left[\frac{K}{3K^o}\delta_{ij}\delta_{pp} + \frac{\mu}{3K^o}\left(\delta_{ij} + \delta_{ij} - \frac{2}{3}\delta_{ij}\delta_{pp}\right)\right] \qquad = \delta_{ij} - \frac{K}{K^o}\delta_{ij}$$

Finally, for isotropic poroelastic media, we have:

$$\alpha_{ij} = \left(1 - \frac{K}{K^o}\right)\delta_{ij} \tag{3.12}$$

This expression (3.12) exactly corresponds to the formulae obtained in the paper of Nur and Byerlee (1971).

Cubic symmetry

For the Cubic symmetry, we receive,

$$\alpha_{ij} = \left\{1 - I_1^0\left(C_{11} + C_{12}\right)\right\}\delta_{ij} \tag{3.13}$$

$$\alpha_{11} = \alpha_{22} = \alpha_{33} = 1 - \left\{I_1^0\left(C_{11} + C_{12}\right)\right\}$$

where $I_1^0 = S_{11}^0 + 2S_{12}^0$

Hexagonal symmetry

Case 1: Let's assume that the skeleton material is an isotropic medium, and the effective medium has TI symmetry. The anisotropy is caused by the aligned pores. Then, utilizing equation (3.11) into the equation (3.8), we receive

$$\begin{aligned} \alpha_{11} = \alpha_{22} &= 1 - \frac{\left(C_{11} + C_{12} + C_{13}\right)}{3K^{o}} \\ \alpha_{33} &= 1 - \frac{\left(2C_{13} + C_{33}\right)}{3K^{o}} \end{aligned} \tag{3.14}$$

Case 2: If both the skeleton and effective medium are transversely isotropic with a vertical axis of symmetry, then,

$$\begin{aligned} \alpha_{11} = \alpha_{22} &= 1 - \left\{ I_1^0 \left(C_{11} + C_{12}\right) + I_3^0 C_{13} \right\} \\ \alpha_{33} &= 1 - \left\{ 2I_1^0 C_{13} + I_3^0 C_{33} \right\} \end{aligned} \tag{3.15}$$

where $I_1^0 = S_{11}^0 + S_{12}^0 + S_{13}^0$ and $I_3^0 = 2S_{13}^0 + S_{33}^0$

Orthorhombic symmetry

In this case,

$$\begin{aligned} \alpha_{11} &= 1 - \left\{ I_1^0 C_{11} + I_2^0 C_{12} + I_3^0 C_{13} \right\} \\ \alpha_{22} &= 1 - \left\{ I_1^0 C_{12} + I_2^0 C_{22} + I_3^0 C_{23} \right\} \\ \alpha_{33} &= 1 - \left\{ I_1^0 C_{13} + I_2^0 C_{23} + I_3^0 C_{33} \right\} \end{aligned} \tag{3.16}$$

$$
\begin{aligned}
&I_1^0 = S_{11}^0 + S_{12}^0 + S_{13}^0 \\
\text{where, } &I_2^0 = S_{12}^0 + S_{22}^0 + S_{23}^0 \\
&I_3^0 = S_{13}^0 + S_{23}^0 + S_{33}^0
\end{aligned}
$$

These expressions (3.15) and (3.16) are similar to the expressions received by Cheng (1997).

3.3 Influence of stress on the Biot tensor (α_{ij}): Static case

Let's consider an elastic potential, W (Biot, 1962), such that

$$W = W(\varepsilon_{ik}, \xi)$$

Here, ε_{ik} is the deformation of the solid skeleton, and ξ is the deformation of liquid in the pores.

Then, by definition, the applied stress is, $\sigma_{ik} = \dfrac{\partial W}{\partial \varepsilon_{ik}}$ and the pore pressure, $P = \dfrac{\partial W}{\partial \xi}$

Now, let's consider the full differential of stress and pore pressure

$$
\begin{aligned}
&d\sigma_{ik} = d\sigma_{ik}\left(\varepsilon_{ik}, \xi\right) \\
&dP = dP\left(\varepsilon_{ik}, \xi\right)
\end{aligned}
\tag{3.17}
$$

So, the stress and pore pressure both contribute to the deformation of the solid frame as well as fluid displacement. We can write

$$
\begin{aligned}
d\sigma_{ik} &= \frac{\partial \sigma_{ik}}{\partial \varepsilon_{jl}} d\varepsilon_{jl} + \frac{\partial \sigma_{ik}}{\partial \xi} d\xi \\
&= C_{ikjl} d\varepsilon_{jl} - \alpha_{ik} G d\xi
\end{aligned}
\tag{3.18}
$$

And,

$$dP = \frac{\partial P}{\partial \varepsilon_{jl}} d\varepsilon_{jl} - Gd\xi \tag{3.19}$$

where, $G = \frac{\partial P}{\partial \xi}$ is the modulus of elasticity of liquid. We placed a minus in (3.18) and (3.19), as confining pressure and pore pressure, act oppositely.

From the last equation, we can express that

$$d\xi = \frac{1}{G}\frac{\partial P}{\partial \varepsilon_{ik}} d\varepsilon_{ik} - \frac{1}{G} dP \tag{3.20}$$

Substitution of (3.20) into (3.18) leads:

$$\begin{aligned} d\sigma_{ik} &= C_{ikjl} d\varepsilon_{jl} - \alpha_{ik} (\frac{\partial P}{\partial \varepsilon_{jl}} d\varepsilon_{jl} - dP) \\ &= (C_{ikjl} - \alpha_{ik} \frac{\partial P}{\partial \varepsilon_{jl}}) d\varepsilon_{jl} + \alpha_{ik} dP \\ &= \tilde{C}_{ikjl} d\varepsilon_{jl} + \alpha_{ik} dP \end{aligned} \tag{3.21}$$

As follows from formulae (3.21), elastic constants are not dry already and depend on the pore pressure and effective stress. It is called effective instead of applied because there is a liquid in our case.

3.3.1 Isotropic medium under pressure

Let's investigate formula (3.8) and consider an isotropic case where pressure is applied to an intrinsic isotropic rock. In this case (Nur and Byerlee, 1971),

$$\alpha = 1 - \frac{\tilde{K}}{K^o} = 1 - \tilde{K}S^o \tag{3.22}$$

where, $S^o = \dfrac{1}{K^o}$

Let's suppose that $\tilde{K}$ is a function of effective pressure ($P_e = P_c - \alpha P$), where the confining pressure (P_c) is $\frac{1}{3}\sigma_{ii}$. We take $\tilde{K}_1$ as a constant such that $\tilde{K} = \tilde{K}_1$ at a certain depth and particular stress. Now, we write,

$$\tilde{K} = \tilde{K}_1 + \tilde{K}_2 \tag{3.23}$$

where $\tilde{K}_2$ is a function of $(P_c - \alpha P)$

And, therefore

$$\tilde{K} = \tilde{K}_1 + K_2 - \alpha K_3 \tag{3.24}$$

Where $\tilde{K}_1$ is the bulk modulus of the dry rock, K_2 is the bulk modulus due to the added confining pressure, and K_3 is the elastic modulus related with the coupled solid deformation and fluid incompressibility due to the pore pressure. The K_3 modulus can be found by solving the equation (3.20) . Our goal of this section was to present a simple equation due to the increase of confining pressure and pore pressure. Detailed studies of K_3 equivalent parameters are available in the literature, such as parameter M in Cheng (1997).

Substitution of (3.24) into (3.22) gives

$$\alpha = 1 - S^o \tilde{K}_1 - S^o K_2 + S^o K_3 \alpha \tag{3.25}$$

Or,

$$\alpha = \frac{1 - S^o \left(\tilde{K}_1 + K_2 \right)}{1 - S^o K_3} \tag{3.26}$$

It is easy to see that (3.26) becomes (3.22), as K_2 and K_3 equals 0 with no additional confining pressure or pore pressure.

3.3.2 Isotropic medium under uniaxial stress

The stress state within the Earth is described by a stress tensor that varies depending on the overburden of the rock layers, tectonic setting, and the pressure exerted by the pore fluid. The stress in a medium induce changes in elastic constants and may result in anisotropy of elastic wave velocities. Many theories and empirical equations have been proposed over the years to establish the relations between elastic constants and stress. Here we utilize a phenomenological approach given by Nikitin and Chesnokov (1981) for an elastic medium and extended by Chesnokov et al. (2002) for a poroelastic rock to link elastic constants (also seismic wave velocities) with stress. Let us start with a Piola-Kirchhoff stress tensor by writing it as a sum of the spherical part and deviating part.

$$\tau_{ij}^0 = -P\delta_{ij} + t_{ij}^0 \tag{3.27}$$

where $P = \left(-\tau_{ii}^0 / 3 \right)$, and t_{ij}^0 is the deviation of the initial stress tensor. The transformation between the Piola-Kirchhoff tensor and Cauchy stress tensor is available in various texts (Bland, 1969;

Liao, 2012). The stiffness tensor for a medium with initial stresses has the following form (Nikitin and Chesnokov, 1981)

$$C_{ijkl} = C_{ijkl}^{p}\left(P_c\right) + B_{ijklmn} t_{mn}^{o} \tag{3.28}$$

where C_{ijkl}^{p} is a function of the confining pressure (P_c); and B_{ijklmn} is the part of the elastic moduli characterizing the anisotropy of the medium created by the initial stress. We must note that the tensor B_{ijklmn} (Nikitin and Chesnokov, 1981) is different from the so-called third-order elastic tensor C_{ijklmn} (Thurston and Brugger, 1964). The connection between C_{ijklmn} and B_{ijklmn} is presented in the following section.

The equation for the elastic moduli of an isotropic medium under stress is

$$C_{ijkl}\left(t_{mn}^{o}\right) = \lambda\left(P_c\right)\delta_{ij}\delta_{kl} + \mu\left(P_c\right)(\delta_{ik}\delta_{jl} + \delta_{il}\delta_{jk}) + \nu_1(\delta_{ij}t_{kl}^{o} + \delta_{kl}t_{ij}^{o}) + \frac{1}{2}\nu_2\{(\delta_{ik}t_{jl}^{o} + \delta_{il}t_{jk}^{o}) + +(\delta_{jl}t_{ik}^{o} + \delta_{jk}t_{il}^{o})\} \tag{3.29}$$

where λ and μ are pressure (P_c) dependent Lamé coefficients; ν_1 and ν_2 are the independent and non-zero components of the tensor B_{ijklmn} .

Let's assume uniaxial stress applied vertically such that $-t_{11}^{0} = -t_{22}^{0} = \frac{1}{2}t_{33}^{0}$, the components of stiffness tensor should follow connections such as

$$\begin{aligned}
(C_{11} - C_{22}) &= 2(C_{13} - C_{23}) + 4(C_{55} - C_{44}) \\
(C_{11} - C_{33}) &= 2(C_{12} + C_{23}) + 4(C_{66} - C_{44}) \\
(C_{11} + C_{22} + C_{33}) &= (C_{12} + C_{23} + C_{13}) + 2(C_{44} + C_{55} + C_{66})
\end{aligned} \tag{3.30}$$

Therefore, isotropic media under stress results in TI media.

Now, we apply the equation (3.28) for a poroelastic media under stress in (3.8), and rewrite (3.8) as

$$\alpha_{ij} = \delta_{ij} - \tilde{C}_{ijkl} S^{o}_{klmm} \tag{3.31}$$

Where, $\tilde{C}_{ijkl}\left(\sigma_{qp}\right) = C^{p}_{ijkl} + B_{ijklqp} t^{o}_{qp}$

and, $t^{o}_{qp} = \sigma_{qp} - \alpha_{qp} P$

We write equation (3.31) more explicitly as

$$\alpha_{ik} = \delta_{ik} - C_{ikjl} S^{o}_{jlmm} - B_{ikjlqp} t^{o}_{qp} S^{o}_{qlmm} \tag{3.32}$$

3.4 The connection between the third-order approximation of nonlinear elastic tensor (C_{ijklmn}) and B_{ijklpq}

This section shows a link between the two classes of theories (Rasolofosaon, 1998) available for the investigation of the effect of stress on elastic bodies. The first class of theory assumes that the pre-stress in the elastic body is achieved by reversible processes (Thurston and Brugger, 1964; Thurston, 1965; Rasolofosaon, 1998). In the second theory, the stress magnitude is considered small compared to the elastic moduli, and no assumptions are made about the processes that result in initial stress (Dahlen, 1972; Nikitin and Chesnokov, 1981; Nikitin and Chesnokov, 1984). A connection between the elastic tensors of the two theories is given below.

Let's consider the wave equation

$$\rho \frac{\partial^2 U_i}{\partial t^2} = \frac{\partial}{\partial x_j} \sigma_{ij} \tag{3.33}$$

where, ρ is the density of the medium, U_i is the displacement and

$$\sigma_{ij} = C_{ijkl} \varepsilon_{kl} \tag{3.34}$$

Here σ_{ij} is the stress tensor, C_{ijkl} is the stiffness tensor and ε_{kl} is the strain tensor.

In a case of paper Nikitin and Chesnokov (1981), the expression (3.34) has the form:

$$\sigma_{ij} = C_{ijkl} \varepsilon_{kl} = \left\{ C^0_{ijkl}(P) + B_{ijklpq} t^0_{pq} \right\} \varepsilon_{kl} \tag{3.35}$$

where C^0_{ijkl} is a function of pressure (P), t^0_{pq} is the deviation of the initial stress tensor and B_{ijklpq} is the elastic moduli characterizing the anisotropy of the medium resulting from the initial stress.

The nonlinear relationship between σ_{ij} and ε_{jl} (Thurston and Brugger, 1964) has the form:

$$\sigma_{ij} = C_{ijkl} \varepsilon_{kl} = \left\{ C^0_{ijkl} + C_{ijklmn} \varepsilon_{mn} \right\} \varepsilon_{kl} \tag{3.36}$$

Presenting ε_{kl} as:

$$\varepsilon_{kl} = \varepsilon^0_{kl} + \varepsilon^1_{kl} \tag{3.37}$$

Substituting (3.36) into (3.33) and using (3.37), we obtain

$$\rho \frac{\partial^2 U_i}{\partial t^2} = \frac{\partial}{\partial x_j} \left\{ \left[C^0_{ijkl} + C_{ijklmn} \varepsilon_{mn} \right] \varepsilon_{kl} \right\} \tag{3.38}$$

or:

$$\rho \frac{\partial^2 U_i}{\partial t^2} = \frac{\partial}{\partial x_j} \left\{ \left[C^0_{ijkl} + C_{ijklmn} \varepsilon^0_{mn} \right] \varepsilon^1_{kl} \right\} + \frac{\partial}{\partial x_j} C_{ijklmn} \varepsilon^1_{mn} \varepsilon^0_{kl} \tag{3.39}$$

The expression (3.39) can be written in the form

$$\rho \frac{\partial^2 U_i}{\partial t^2} = \frac{\partial}{\partial x_j}\left\{\left[C^0_{ijkl}\varepsilon^1_{kl}\right]\right\} + \frac{\partial}{\partial x_j}\left\{\left[C_{ijklmn}\varepsilon^0_{mn}\right]\varepsilon^1_{kl}\right\} + \frac{\partial}{\partial x_j} C_{ijklmn}\varepsilon^1_{mn}\varepsilon^0_{kl} \tag{3.40}$$

Taking into account that

$$\varepsilon^1_{mn} = \delta_{km}\delta_{\ln}\varepsilon^1_{kl} \tag{3.41}$$

The formula (3.40) can be rewritten as

$$\begin{aligned}
\rho \frac{\partial^2 U_i}{\partial t^2} &= \frac{\partial}{\partial x_j}\left\{\left[C^0_{ijkl}\varepsilon^1_{kl}\right]\right\} + \frac{\partial}{\partial x_j}\left\{\left[C_{ijklmn}\varepsilon^0_{mn}\varepsilon^1_{kl}\right]\right\} + \frac{\partial}{\partial x_j} C_{ijklmn}\delta_{jm}\delta_{\ln}\varepsilon^1_{kl}\varepsilon^0_{kl} \\
&= \frac{\partial}{\partial x_j}\left\{C^0_{ijkl}\varepsilon^1_{kl}\right\} + 2\frac{\partial}{\partial x_j}\left\{C_{ijklmn}\varepsilon^0_{mn}\varepsilon^1_{kl}\right\} \\
&= \frac{\partial}{\partial x_j}\left\{[C^0_{ijkl} + 2C_{ijklmn}\varepsilon^0_{mn}]\varepsilon^1_{kl}\right\}
\end{aligned} \tag{3.42}$$

Hooke's law for the linear part of deformation has the form

$$\varepsilon^0_{mn} = S^0_{mnpq}\tau_{pq} \tag{3.43}$$

Substitution (3.43) into (3.42) leads to the expression:

$$\rho \frac{\partial^2 U_i}{\partial t^2} = \frac{\partial}{\partial x_j}\left\{[C^0_{ijkl} + 2C_{ijklmn}S^0_{mnpq}\tau_{pq}]\varepsilon^1_{kl}\right\} \tag{3.44}$$

Comparison between (3.35) and (3.36) with taking into account (3.44) gives:

$$B_{ijklpq} = 2C_{ijklmn}S^0_{mnpq} \tag{3.45}$$

Under conditions:

$$C^0_{ijkl} = C^0_{ijkl}(P) \tag{3.46}$$

And, the deviatoric stresses

$$\tau_{pq} = t_{pq}^0 \tag{3.47}$$

3.5 Dynamic case: Frequency dependence

In this section, we derive the macroscopic equation for an anisotropic poroelastic medium, saturated with liquid of low viscosity (Chesnokov et al., 2019). To this end, as an initial point, we use a microscopic motion equation for the centroid of a physically infinitely small volume of poroelastic media, which contains a linked system of randomly distributed pores filled with viscous liquid.

$$\frac{\partial}{\partial x_j}\left\{C_{ijkl}\left[1-\chi\left(\vec{x}\right)\right]-i\omega\eta\chi\left(\vec{x}\right)\delta_{jk}\delta_{il}\right\}\frac{\partial}{\partial x_k}u_l\left(\omega,\vec{x}\right)=\frac{\partial}{\partial x_i}\chi\left(\vec{x}\right)P_f\left(\omega,\vec{x}\right) \tag{3.48}$$

where C_{ijkl} is the stiffness tensor of the material, η is the viscosity of the pore fluid, P_f is the Fourier transform of pore pressure, and δ is the well-known Kronecker delta. The characteristic multitude function $\chi(\vec{x})$ equals one if point $\vec{x}$ belongs to the area taken by the liquid and equals zero if this point belongs to the area taken by the skeleton. The Fourier image of the medium deformation vector in the Fourier domain is $u_l\left(\omega,\vec{x}\right)$. For simplicity, we will only consider the case of low frequency ($\omega < \frac{\eta}{\rho\kappa}$), where ρ is the average density and κ is the permeability of the medium.

The deformation response of the medium at a set pressure is

$$u_i(\omega,\vec{x}) = \int G_2^i(\vec{x},\vec{x}\,')P_f(\vec{x}\,')d\vec{x}\,' \tag{3.49}$$

where

$$G_2^i(\vec{x},\vec{x}\,') = G_1^{ij}(\vec{x},\vec{x}\,')\frac{\partial}{\partial x_j'}\chi(\vec{x}\,') \tag{3.50}$$

is the differential operator over the argument $\vec{x}'$which affects not only the function $\chi(\vec{x}')$ but also $P_f(\vec{x}')$. In the equation (3.50), $G_1^{ij}(\vec{x},\vec{x}')$ is the Green function which satisfies the following equation

$$\frac{\partial}{\partial x_j}\left\{C_{ijkl}\left[1-\chi(\vec{x})\right]-i\omega\eta\chi(\vec{x})\delta_{jk}\delta_{il}\right\}\frac{\partial}{\partial x_k}G_1^{lm}(\vec{x},\vec{x}\,') = \delta_{im}\delta(\vec{x}-\vec{x}\,') \tag{3.51}$$

where $\delta(\vec{x}-\vec{x}')$ is the Dirac delta function.

The mean value of the Green function $G_1^{ij}(\vec{x},\vec{x}')$ describes the mean value of the medium deformation vector. We assume the pore pressure in the low-frequency range as a set function of the coordinates, which is defined only by external forces. Note that the Green function depends not only on the elasticity moduli but also on liquid viscosity, which differs from the low viscosity liquid case considered in Biot theory (1962).

To average equations (3.49) to (3.51), we will be using diagram technique analogous to the ones applied for effective parameters of a statistically random inhomogeneous elastic media (Rytov et al., 1989; Chesnokov et al., 1995; Bayuk and Chesnokov, 1998) and poroelastic media (Chesnokov et al., 2002). The result of this averaging is the Dyson equation of Green function;

$$\bar{G}_1^{ik}(\vec{x},\vec{x}\,')=G_0^{ik}(\vec{x},\vec{x}\,')+\int G_0^{ij}(\vec{x},\vec{x}_1^{\,'})\Sigma_1^{jl}(\vec{x}_1^{\,'},\vec{x}_2^{\,'})\bar{G}_1^{lk}(\vec{x}_1,\vec{x}_2^{\,'})d\vec{x}_1,d\vec{x}_2^{\,'} \tag{3.52}$$

where $\bar{G}_1^{ik}(\vec{x},\vec{x}')$ is averaged Green function, $G_0^{ik}(\vec{x},\vec{x}')$ satisfies equation (3.50) if χ=0, $\Sigma_1^{jl}(\vec{x}_1',\vec{x}_2')$ -correlation operator represented by an infinite series of diagrams containing a "perturbation" operator.

$$\frac{\partial}{\partial x_j}\left\{C_{ijkl}+i\omega\eta\delta_{jk}\delta_{il}\right\}\chi(\vec{x})\frac{\partial}{\partial x_k}$$

The summation of the Dyson series for the average Green function can be performed through the effective operator in an analytical form by incorporating the n-point correlation functions proposed by Vikhorev and Chesnokov (2009). This method is particularly suitable when considering attenuation due to scattering.

In the same way, we obtain the averaged response of the medium to the gradient of porous pressure.

$$\bar{G}_2^{i}(\vec{x},\vec{x}\,')=\int \bar{G}_1^{ik}(\vec{x},\vec{x}\,')\Sigma_2^{k}(\vec{x}_1,\vec{x}\,')d\vec{x}_1 \tag{3.53}$$

where $\Sigma_2^k(\vec{x}_1,\vec{x}')$ is the second correlation operator. Its application allows the generalized non-local Biot-Willis parameter $\alpha^{ij}(\omega,\vec{x}_1,\vec{x})$ to be defined by the following equation:

$$\Sigma_2^{l}(\vec{x},\vec{x}\,')=-\frac{\partial}{\partial x_j}\alpha^{ij}(\omega,\vec{x},\vec{x}\,') \tag{3.54}$$

The first correlation operator $\Sigma_1^{jl}(\vec{x}_1',\vec{x}_2')$ is linked with the effective tensor of elastic moduli of a poroelastic medium which is saturated with a viscous liquid, C_{ijkl}^*.

From here we deduce the link between the full stress tensor σ_{ij} and the effective stiffness tensor C^*_{ijkl} and the pore pressure:

$$\sigma_{ij}\left(\vec{x}\right)=\int C^*_{ijkl}\left(\omega,\vec{x},\vec{x}'\right)\frac{\partial}{\partial x_k}u_l\left(\vec{x}\right)d\vec{x}'+\int \alpha^{ij}\left(\omega,\vec{x},\vec{x}'\right)P_f\left(\vec{x}'\right)d\vec{x}' \tag{3.55}$$

It should be noted that the case of viscous liquid $\alpha^{ij}(\omega,\vec{x},\vec{x}')$ depends on frequency and is a complex function. By taking into account the link between $\Sigma_1^{jl}(\vec{x}_1',\vec{x}_2')$ and $\Sigma_2^{k}(\vec{x}_1,\vec{x}')$ it is possible to express the Biot-Willis parameter through the effective stress tensor for a poroelastic medium saturated with viscous liquid.

$$\alpha^{ij}\left(\omega,\vec{x},\vec{x}'\right)=\delta_{ij}\delta\left(\vec{x}-\vec{x}'\right)-C^*_{ijkl}\left(\omega,\vec{x},\vec{x}'\right)S_{klmn} \tag{3.56}$$

where S_{klmn} is the inverse tensor of $C_{ijkl}+i\omega\eta\delta_{jk}\delta_{il}$

Therefore, based on the proposed microscopic equation for a deformation of a poroelastic medium saturated with viscous liquid, it is possible to generalize Biot theory and to obtain the effective stress tensor and Biot-Willis parameter in the case of random viscosity. However, we focus on the homogeneous Newtonian fluid in this study. Therefore, the liquid is a mixture of water and oil with only bulk moduli of the fluid. And the seismic dispersion comes from the scattering of the inclusions. On the basis of the diagram technique, we obtained an expression for the Biot-Willis parameter, which allows us to calculate it in the dynamic range. We received the expression for the Biot-Willis parameter in the general non-local case when the Fourier image of this parameter depends not only on frequency but also on the wave vector. In the threshold case, when the length of elastic waves is much higher than the characteristic size of random inhomogeneities, integral expression (3.55) turns into finite expression.

$$\sigma_{ij}\left(\vec{x}\right)=C^{*}_{ijkl}\left(\omega,\vec{x}\right)\frac{\partial}{\partial x_k}u_l\left(\omega,\vec{x}\right)+\alpha^{ij}\left(\omega,\vec{x}\right)P_f\left(\omega,\vec{x}\right) \tag{3.57}$$

And , $\alpha_{ik}\left(\omega,\vec{x}\right)=\delta_{ik}-\tilde{C}_{ijkl}\left(\omega,\vec{x}\right)S^{o}_{jlmm}$ (3.58)

Here, $\tilde{C}_{ijkl}\left(\omega,\vec{x}\right)$ is calculated under the condition of existing liquid in pores.

Chapter 04

Practical Application: Biot tensor in poroelastic media

4.1 Introduction

In this chapter, we demonstrate the implementation of our theoretical equations of chapter three, and we compare our calculations to the available experimental data from the literature. This chapter's content is also a part of the publication (Morshed, Chesnokov and Vikhoreva, 2021) mentioned in chapter three.

We calculated the Biot tensor for different scenarios to support our theoretical formulation, such as changes in confining pressure, pore pressure, and uniaxial stress. We choose sedimentary rocks, for example, sandstone and shale. To ensure maximum accuracy, we pick experimental data from literature where either all data related to poroelastic measurements are provided and microstructural data such as mineralogical composition and porosity are given. A careful selection of data involves information on the details of the experiment and the rock's composition. It is often difficult to find the exact match between the experimental setup and theoretical assumptions beneath the equations. There are also many different methods for measuring the Biot α, especially how strain, stress, and pore pressure are varied during data acquisition. These approaches include quasi-static and ultrasonic measurements. There are two quasi-static methods (Al-Tahini et al. 2005), commonly known as direct method and indirect method. In the direct method, the changes of pore volume and the changes of the bulk volume of a saturated sample are measured as the confining pressure is varied with constant pore pressure. The direct method is also called a jacketed test. The indirect method measures the stiffness moduli (e.g., bulk moduli for isotropic case) of the fluid-saturated rock and the solid matrix's stiffness moduli using an unjacketed test where differential pressure is kept zero (i.e., Pp= Pc). The ultrasonic measurements exploit compressional and shear wave velocities usually measured on dried rock samples.

We also estimated the frequency-dependent Biot tensor for TI models using numerical calculations as such experimental data for dynamic cases is extremely rare.

4.2 Isotropic rock under pressure

In this section, we apply equation 3.26 to compute Biot's coefficient for an isotropic medium due to reservoir pressure changes. We select experimental data (Ma and Zoback 2017) to estimate α for poroelastic stress changes associated with depletion and injection. They used the indirect method of Biot α measurement, and therefore they measured the bulk modulus of the saturated sample and solid matrix. As the solid matrix (i.e., grain bulk modulus) is measured, maintaining confining pressure equal to pore pressure, the grain bulk modulus (Kg or K^o) increases as pore pressure increases. The higher bulk modulus is partly attributed to the stiffening of microfractures as fluid pressure increases. Following our equations (it applies to other methods also), an increase in K^o means higher α. The variation of α of a sample (B9V) is shown in Figure 4.1, Figure 4.2, and Figure 4.3 for three different scenarios: changes in confining pressure only (dry case), decreases in pore pressure at Pc=70 MPa, and changes in both Pc and Pp with constant differential pressure (Pe=Pc-Pp=10MPa). We see a good fit between the experimental data and our computation in all three cases. Our predicted data sometimes underpredicted the experimental data. However, Al-Tahini et al. (2005) reported that the measured Biot coefficient from the indirect method usually has higher values than the more accurate direct method.

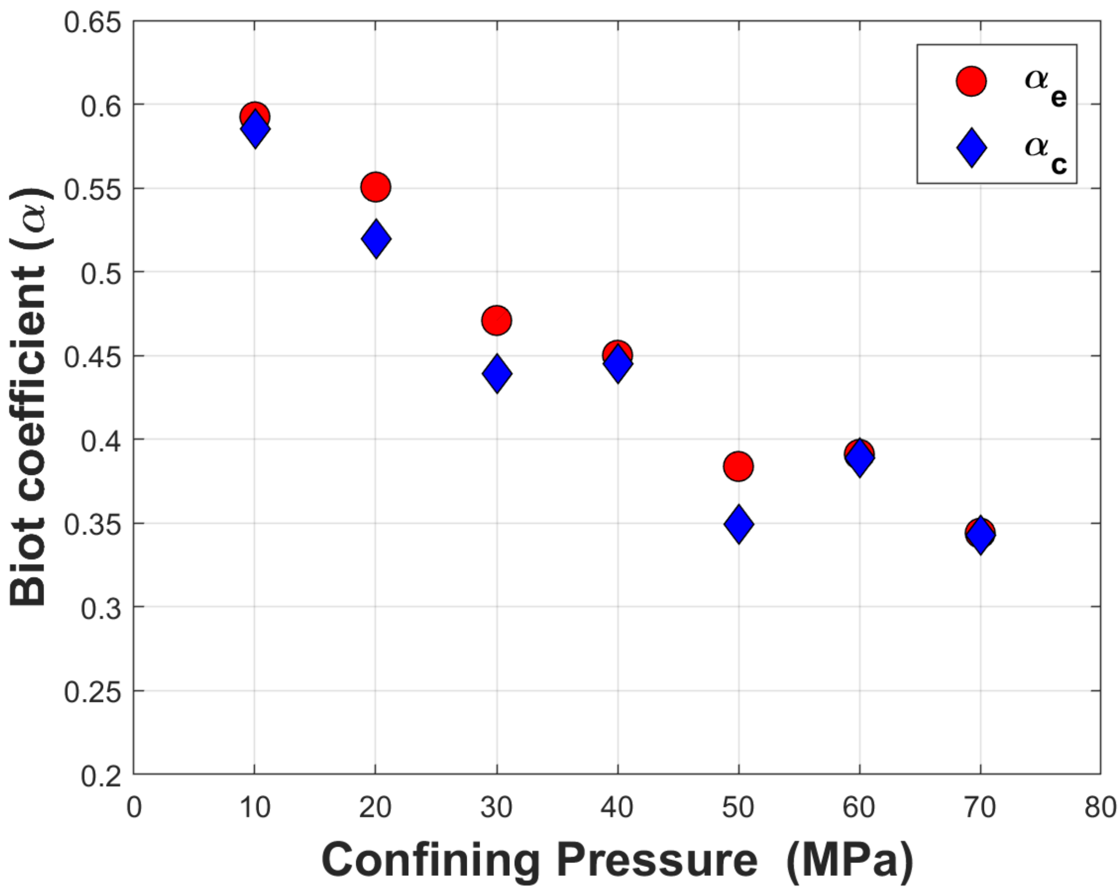

Figure 4.1: The Biot coefficient (α) for confining pressure changes at zero pore pressure of a sandstone (porosity 3.1%) sample. Biot coefficients are calculated from Ma and Zoback (2017) data of a simulated reservoir depletion situation. The measured data is labeled with 'e' and the computed data is labeled with 'c'.

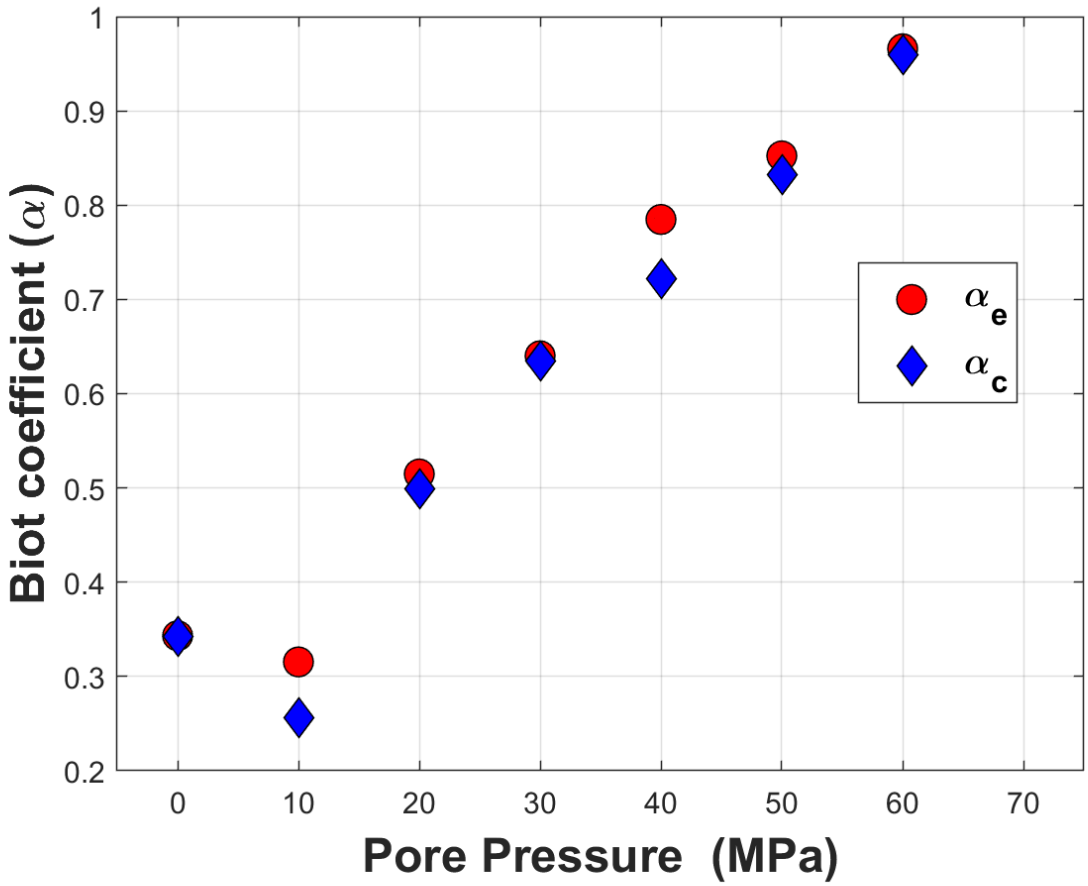

Figure 4.2: The Biot coefficient (α) for pore pressure changes at 70 MPa confining pressure of a sandstone (porosity 3.1%) sample. The α is calculated from Ma and Zoback (2017) data of a reservoir depletion simulated case. The measured data is labeled with 'e' and the computed data is labeled with 'c'.

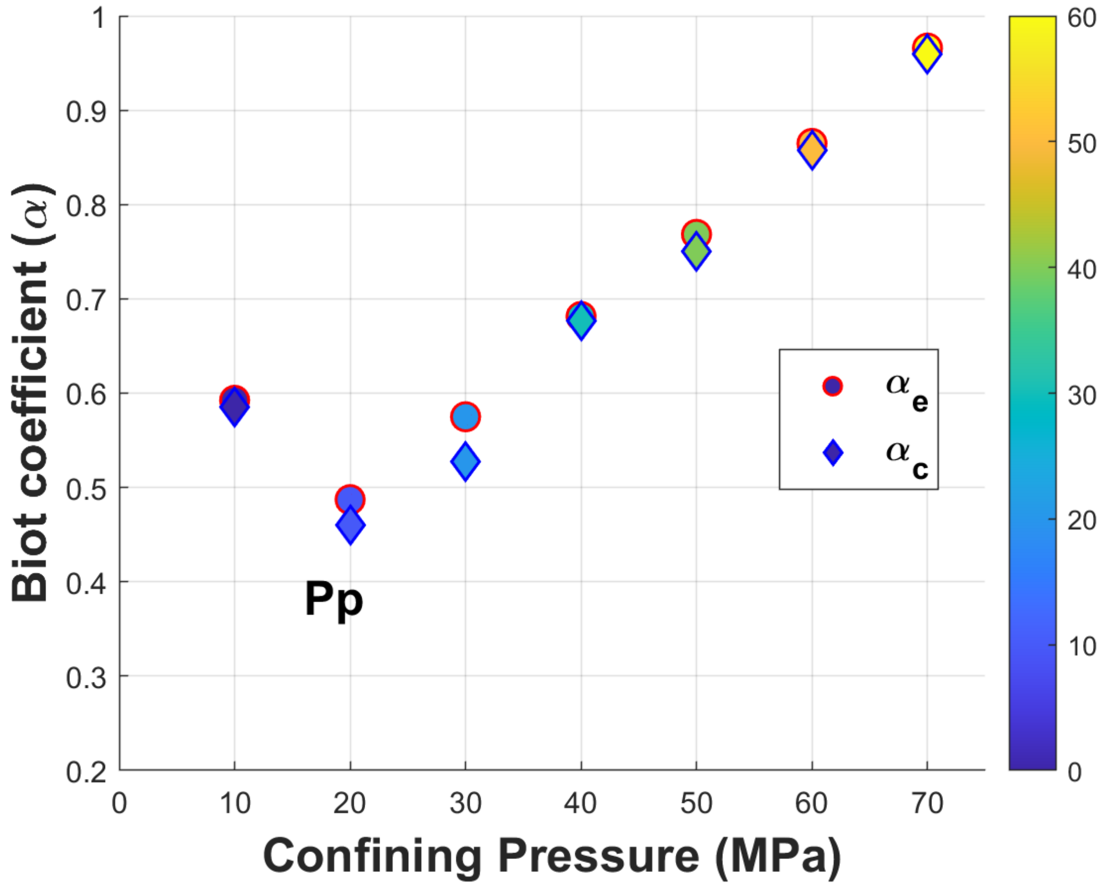

Figure 4.3: The Biot coefficient (α) for changes in both confining pressure and pore pressure at 10 MPa differential pressure of a sandstone (porosity 3.1%) sample. The color bar represents the pore pressure values. The α is calculated from Ma and Zoback (2017) data of a reservoir depletion simulated case. The measured data is labeled with 'e' and the computed data is labeled with 'c'.

4.3 Uniaxial strain to an isotropic rock

We select the ultrasonic data of uniaxial strain experiment of Scott and Abousleiman (2005) to understand the behavior of the Biot tensor for the uniaxial loading situation. They measured ultrasonic velocities on Berea Sandstone under various stress conditions such as hydrostatic, triaxial, and uniaxial strain experiments. The Berea Sandstone is an isotropic and porous monomineralic rock. Therefore, Scott and Abousleiman's data is our choice to investigate the effect of stress on elastic moduli and Biot tensor to an initial isotropic rock. While hydrostatic stress does not generate anisotropy to the elastic and poroelastic parameters of the rock, the uniaxial stain and triaxial stress experiment induce anisotropy to the isotropic rock. The uniaxial strain experiment (i.e., the sample shortens only in one direction) is often known as a good proxy of the in-situ stress conditions of the subsurface (Herwanger and Koutsabeloulis 2011). The uniaxial stress altered the Berea Sandstone to become a transversely isotropic rock with a vertical axis of symmetry (VTI) and caused the most substantial variations of α among the three experiments. We calculated the horizontal and vertical components of α using the formula 3.32, and we plotted those values with uniaxial stress along with the measured data (Figure 4.4). We write the equations for the measured velocities following Nikitin and Chesnokov (1981) as below:

$$
\begin{aligned}
\rho V_{p11}^2 &= \lambda + 2\mu + \left\{2(\nu_1+\nu_2)+1\right\} t_{11}^o - P \\
\rho V_{p33}^2 &= \lambda + 2\mu + \left\{2(\nu_1+\nu_2)+1\right\} t_{33}^o - P \\
\rho V_{s11}^2 &= \mu - 0.5\nu_2 t_{33}^o + t_{11}^o - P \\
\rho V_{s13}^2 &= \rho V_{s23}^2 = \mu - 0.5\nu_2 t_{11}^o + t_{33}^o - P
\end{aligned}
\tag{4.1}
$$

where ρ is the density of the sample, Vp and Vs are the compressional and shear wave velocities, 11 and 33 represent the horizontal and vertical directions, respectively, 13 and 23 represent the propagation of shear waves in the vertical direction. We solve the equations in (4.1) to calculate $t_{11}^{o}, t_{33}^{o}, \nu_1, \nu_2, P, \lambda$ and μ using the known density and velocities. Then, we use the equation 3.29 to estimate the stiffness tensor of the TI rock at given uniaxial stress.

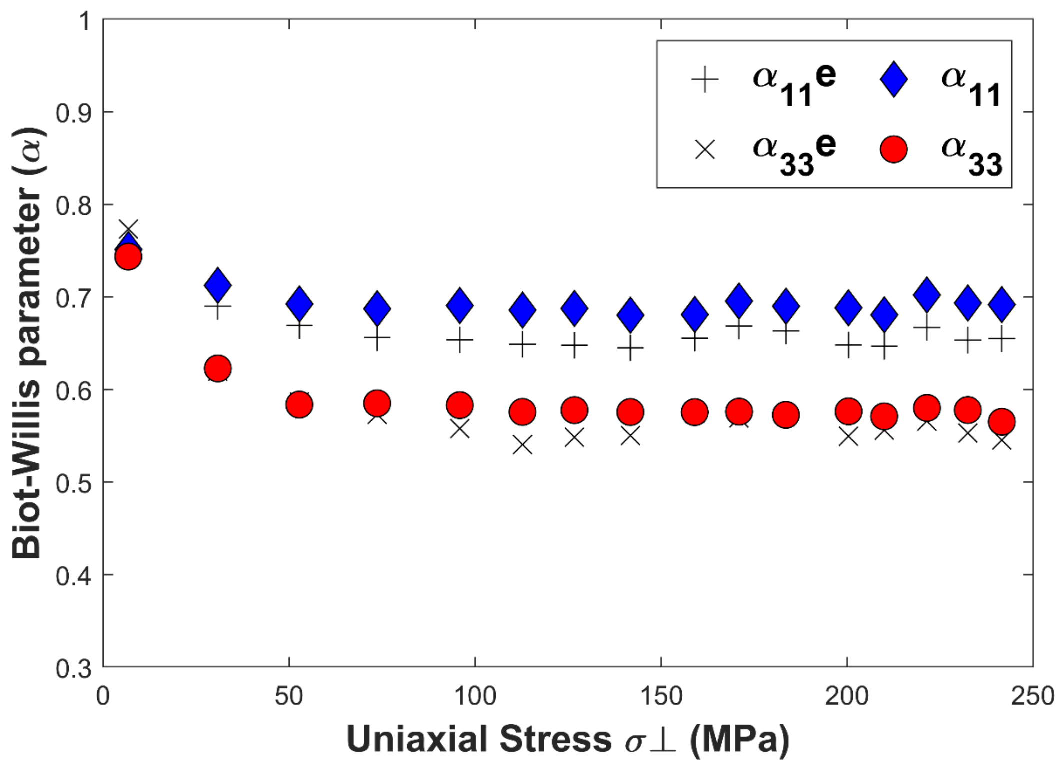

Figure 4.4: The horizontal (α_{11}) and vertical (α_{33}) components of the Biot tensor of stress-induced Transversely Isotropic rock media are shown with uniaxial stress. The measured data is labeled with 'e'. The estimated data using our approach is also shown for the corresponding uniaxial stress.

Let us show an example from the measured velocities at uniaxial load 75.2 MPa with horizontal confining pressure 20.7 MPa. The velocity data are $Vp_{11} = 3.5kms^{-1}$, $Vp_{33} = 3.83kms^{-1}$, $Vs_{11} = 2.26kms^{-1}$ and $Vs_{23} = 2.4kms^{-1}$. Our estimated stress parameters are $t_{11}^{o} = -1.33MPa$, $t_{33}^{o} = 2.66MPa$ and $P = 95.9MPa$.

Both α_{11} and α_{33} initially decrease before reaching constant values beyond 50 MPa as vertically applied uniaxial load increases. In general, our theoretical prediction is in good agreement with the experimental data (Figure 4.4) and α_{33} shows a better fit with measured data than α_{11}. The slight disagreements between experimental values and computed values may arise for several reasons. One of the reasons is related to the data. We do not consider the porosity loss data as such data is not available. However, some porosity loss is expected as the rock sample shrink due to the applied stress (Müller and Sahay 2016). It is also probable to have a little error in data as those are digitized from the graphs of Scott and Abousleiman (2005). Besides, our method works better if more data is available, especially the shear velocities at three perpendicular directions are critical as the stressed rock is expected to have orthorhombic symmetry (Nikitin and Chesnokov 1981; Rasolofosaon 1998).

Moreover, the uniaxial strain test does not allow any strain in horizontal directions. It, therefore, causes greater confinement and a steeper slope of the stress-strain curve than the uniaxial stress case, and some of the applied vertical stress equilibrates throughout the rock (sometimes called quasi-hydrostatic). The ratio of the differential stress to the horizontal confining stress is nearly 3 for the experimental data. However, the theoretical condition to cause the stress-induced TI symmetry is that $t_{11}^{o} = t_{22}^{o} = 0.5t_{33}^{o}$. In other words, uncertainty in the horizontal stresses is also a reason for some mismatch between the experimental data and the theoretical prediction.

4.4 Uniaxial stress to a transversely isotropic rock

In the previous section, we examined the stress-induced change of the Biot tensor. However, rock microstructure also plays a significant role in elastic stiffness and anisotropy. Therefore, pores and minerals' preferred orientation influences the Biot tensor's components, but probably differently than uniaxial stress. So, we estimated α_{11} and α_{33} from our Barnett Shale samples and two TI samples from literature (Sviridov et al. 2017) that have minerals and pores oriented horizontally. All Barnett Shale samples except one show smaller α_{11} compared to α_{33} (Figure 4.5). Therefore, Barnett Shale samples show the opposite trend of what we observed for stressed-induced anisotropy data. However, such behavior is intuitively understandable as uniaxial stress stiffens the rock in the vertical direction, and horizontally aligned microstructure stiffens the rock in the horizontal direction for a VTI rock.

Sviridov et al. (2017) measured ultrasonic velocities while varying uniaxial stress. The sample BaZ is a diagenetically consolidated Siltstone containing 33% Muscovite, 29% Quartz, 33% Chlorite, and 4% porosity. The other sample (DH06) is Clayey bituminous marl containing 33% Calcite, 28% Quartz, 12% Mica, 4% Pyrite, and 23% porosity. To compute the Biot tensor, we inverted the velocities of the ultrasonic measurements for the stress and then estimated the stiffness of the dry rock at each stress point. We computed the stiffness of the skeleton using the General Singular Approximation (GSA) method (Shermergor 1977; Bayuk and Chesnokov 1998; Chesnokov et al. 2009) utilizing mineral composition data. The GSA method is a mathematical approach (discussed in detail in chapter 02) to estimate the effective physical properties of anisotropic porous media.

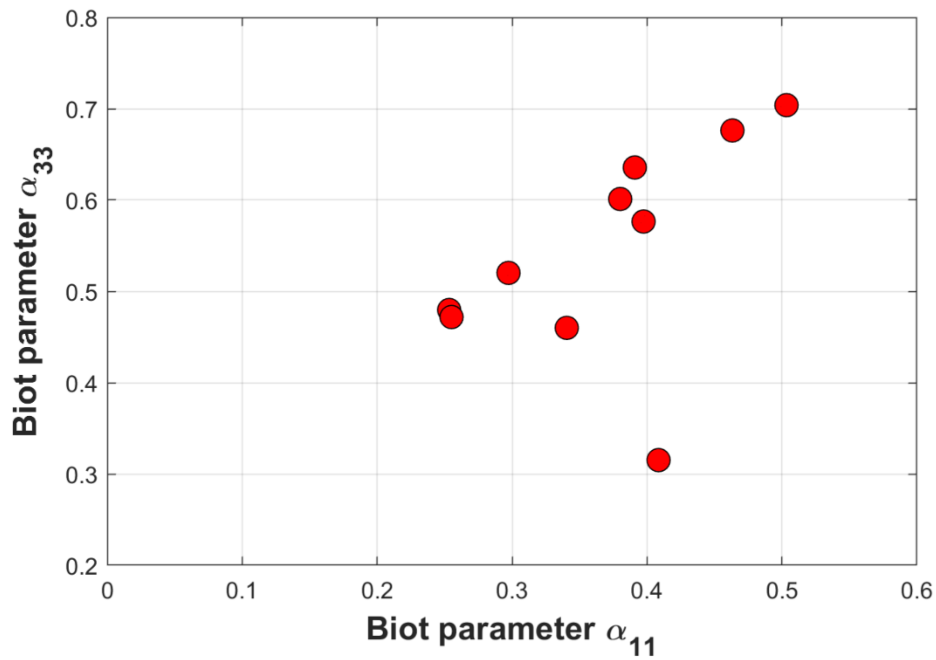

Figure 4.5: The horizontal (α_{11}) and vertical (α_{33}) components of the Biot tensor of Barnett Shale samples are shown.

While calculating components of Biot tensor of the above two transversely isotropic samples, we expect α_{33} lower than α_{11} as we have seen in the previous section as uniaxial stress increases, and the samples are mainly stiffening in the vertical direction. But, the presence of aligned minerals and pores causes higher α_{33} and lower α_{11} for VTI rocks (Figure 4.6). So, the combined effects of stress and oriented microstructure is an intricate issue. Indeed, the decrease of α_{33} for Berea Sandstone is 21% for changes of stress from 6.8 MPa to 30.8 MPa while it is only 4.2 % for BaZ sample for a similar variation of uniaxial stress (5.4 MPa to 31.4 MPa).

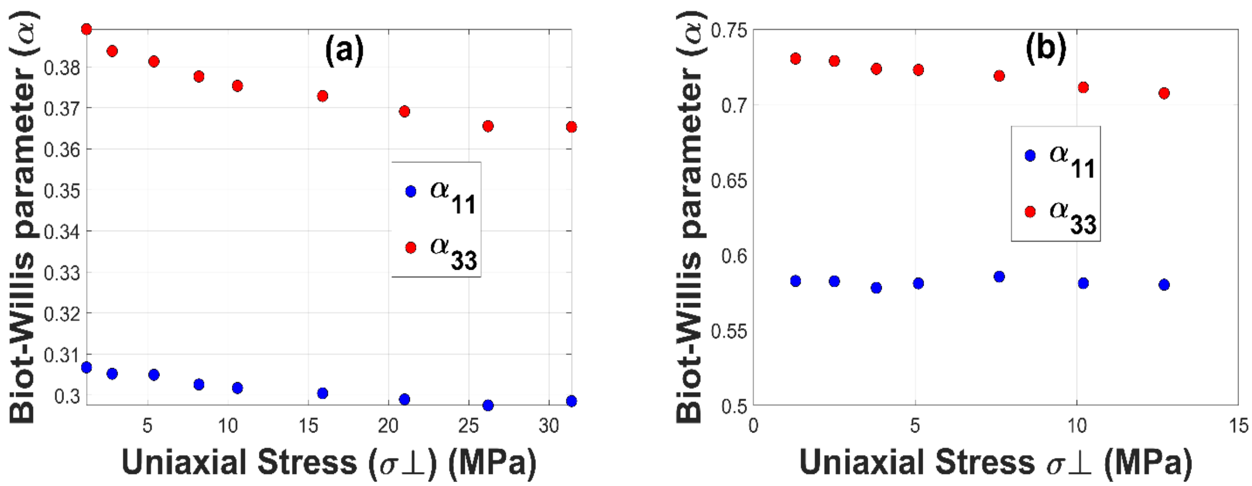

Figure 4.6: The horizontal (α_{11}) and vertical (α_{33}) components of the Biot tensor are shown with applied uniaxial stress for two Shales samples calculated from Sviridov et al. (2017). The left figure represents sample BaZ, and the right figure represents sample DH06. In both cases, α_{11} are smaller than α_{33}.

4.5 Numerical simulations of dynamic case

We perform numerical calculations for the dispersion of seismic waves from four different models. We considered uniformly oriented penny-shaped inclusions (defined by aspect ratios (AR)) with two types of pore fluids (gas and water) in isotropic background medium. We take stress as constant. The diameter (i.e., the long axes of the ellipsoid) of inclusions is 8 mm in all models.

The volume concentration of inclusions is $3x10^{-3}$ and $9x10^{-2}$ for the low aspect ratio (AR=0.004) and high aspect ratio (AR=0.1) models, respectively. All the four models represent effective media (i.e., the wavelength of the seismic waves is much larger than the largest heterogeneities). All the four models represent VTI media as the inclusions are horizontal and uniformly oriented.

We use the algorithm given by Vikhorev and Chesnonov (2009) in an analytical form of the summation of the Green's function for the effective dynamic properties of a randomly inhomogeneous medium based on n-point correlation approximation. The algorithm considers only scattering related attenuation caused by the inclusions. The background medium is taken as isotropic (bulk modulus = 20.34 GPa, shear modulus =17.7 GPa and density =2657 kg/m^3). The bulk moduli of water and gas are taken as 1.4 GPa and 0.01 GPa, respectively.

The variations of velocities of the compressional wave, the fast shear wave, and the slow shear wave are shown as a function of the polar angle in Figure 4.7. The attenuation of P-wave, fast shear wave, and slow shear wave are plotted in Figure 4.8. We also plotted compressional wave anisotropy with frequency in Figure 4.9. The anisotropy coefficient is calculated as A_p=2x (Vp(max)-Vp(min)) / (Vp(max)-Vp(min)) x100% after Vikhorev and Chesnonov (2009). The calculated α_{33} and α_{11} is shown in Figure 4.10 (a) and (b) with changes in frequency. In gas saturated models, both α_{33} and α_{11} initially increase with frequency and reach their maximum at approximately 45 Hz (commonly known to be the band for the surface seismic data), and then decrease with the increase of frequency. The vertical component (α_{33}) is always the most sensitive component in our TI models. For gas saturated small aspect ratio (i.e., 0.004) models, we observe a significant change of α_{33} from 0.49 at 45 Hz to 0.045 at 500 Hz. The α_{33} changes more for compliant inclusion models (AR= 0.004) compared to the stiff inclusion models (AR= 0.1).

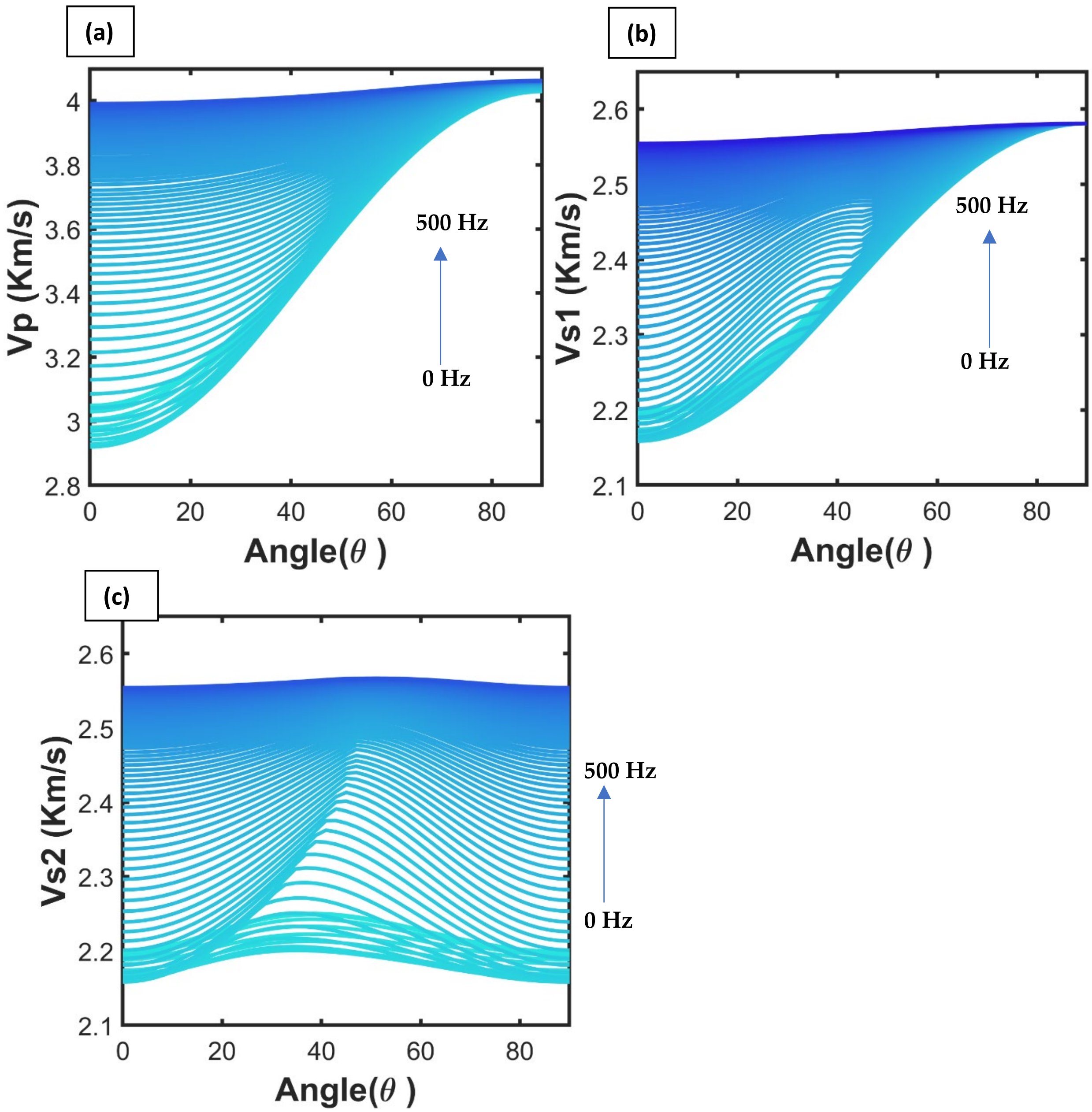

Figure 4.7: The velocities of (a) P-wave, (b) fast shear wave, and (c) slow shear wave are plotted with angles from the symmetry axis for a numerically modeled transversely isotropic medium. The values of frequencies are indicated with an arrow.

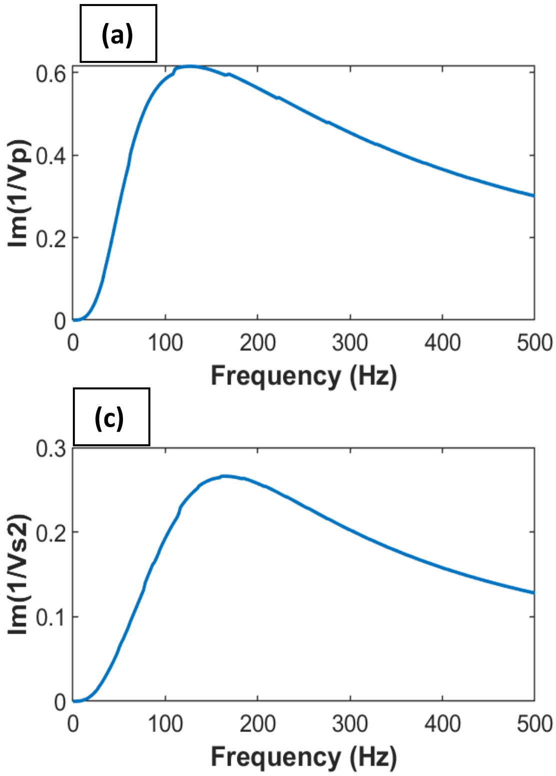

Figure 4.8: The attenuation of (a) P-wave, (b) fast shear wave and (c) slow shear wave are plotted with frequency for the numerically modelled transversely isotropic medium.

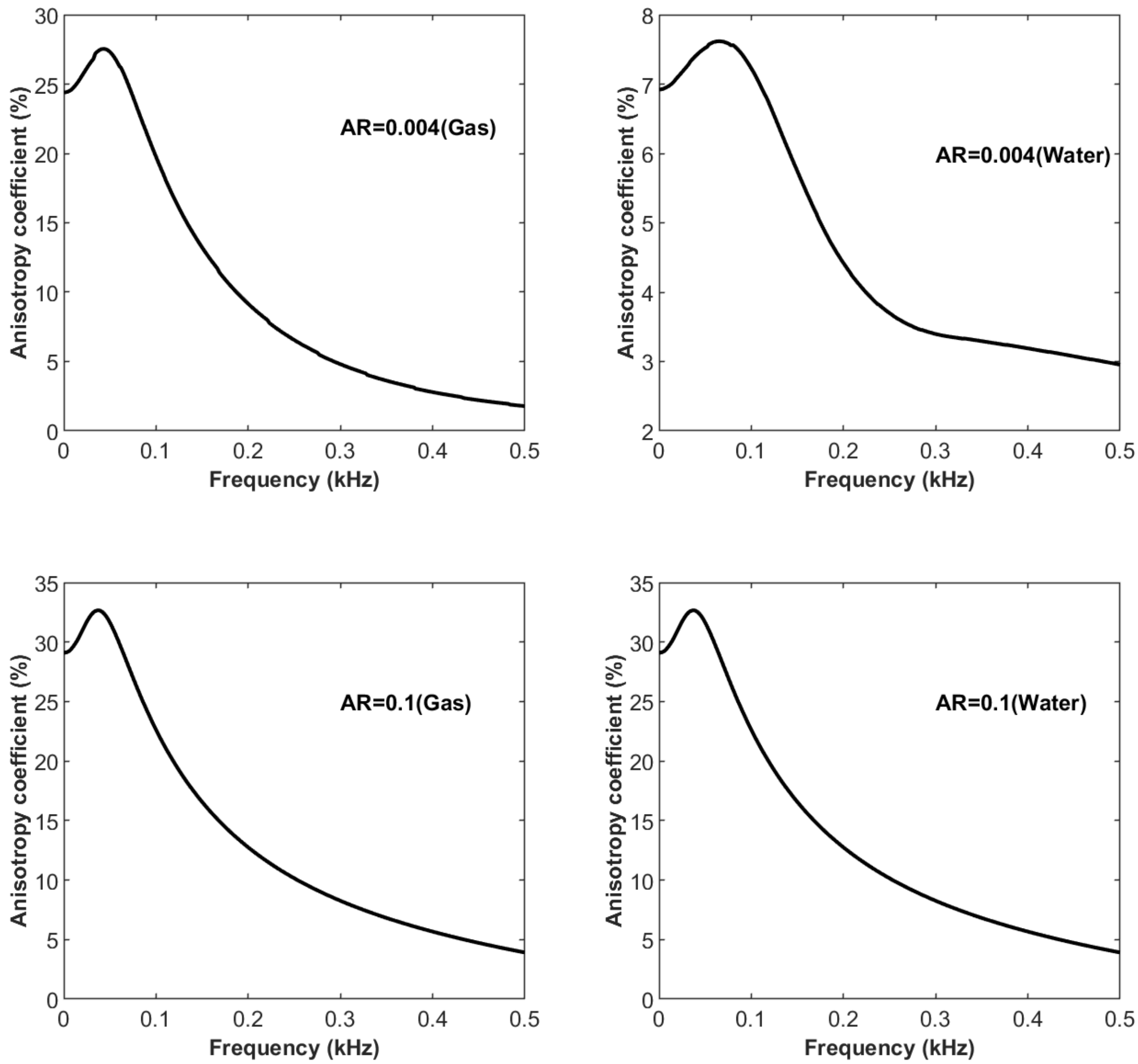

Figure 4.9: The anisotropy coefficient of four models are plotted with frequency. The aspect ratio of inclusions and inclusion fluid are mentioned in each plots.

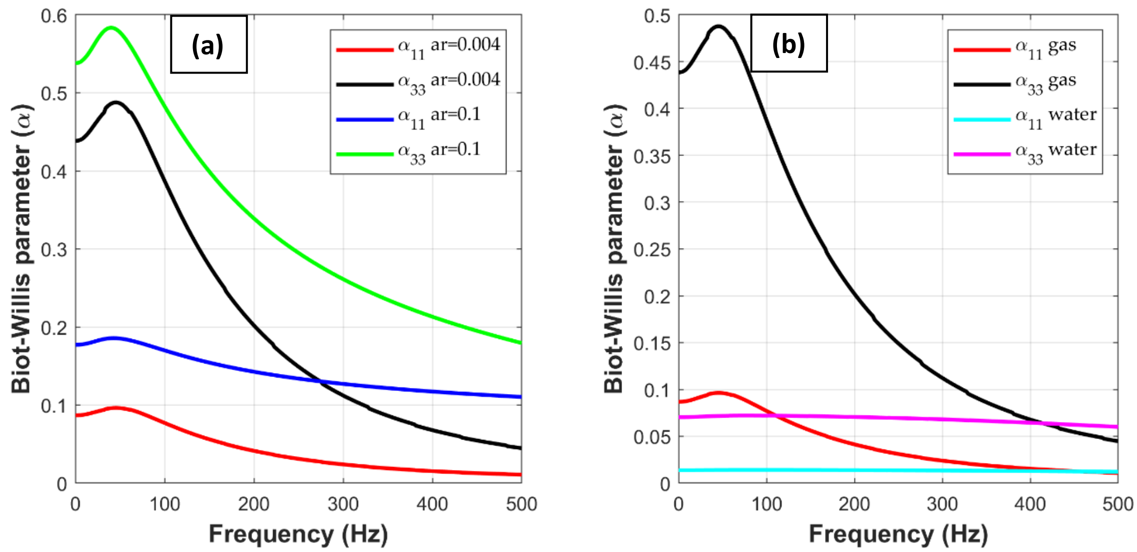

Figure 4.10: The Biot parameters (α_{11} and α_{33}) are plotted as a function of frequency. Figure 4.9(a) shows two models with different aspect ratios (0.004 and 0.1) of the inclusions, and both are gas saturated. Figure 4.9(b) shows two scenarios for gas saturated and water-saturated rocks with aspect ratio 0.004 of the inclusions.

As observed in Figure 4.10 (a) and (b), the variations of Biot α are less for weak contrast inclusion (water-saturated) models compared to the strong contrast (gas saturated) models. The variations of α_{33} and α_{11} are associated with the attenuation of the seismic waves. The attenuation varies with the orientation of the inclusions and the elastic contrast between the matrix and the fluid. The attenuation is maximal in the direction normal to the inclusion planes, and the attenuation is minimal parallel to the inclusion planes (Vikhorev and Chesnonov 2009). Therefore, the frequency of data also plays a vital role in the estimation and interpretation of the Biot tensor. Consequently, a proper method and specific data are necessary to ensure accurate estimation and practical application of the Biot coefficient.

Chapter 5

Summary and Discussion

This research's objective is to understand the stress and frequency-dependent properties of poroelastic anisotropic rocks. We resort to Biot tensor as a linking parameter between stress and microstructure. Therefore, we study the Biot tensor in terms of effective media and frequency-dependent cases for geomechanical and rock physics applications. We derived easily applicable equations to extract the Biot tensor and subsurface stress from elastic moduli in the static case and elastic wave velocities in the dynamic case. We presented an independent derivation of the Biot-Willis tensor for an anisotropic porous medium. We obtained explicit equations for the influence of stress on the Biot tensor. We also provided functional equations of Biot tensor, including non-linear part of stiffness tensor for uniaxial stress cases distinguishing the effect of pressure and deviating part of initial stress.

The Biot parameter measures the compressibility of the rock skeleton with respect to the solid grain (Al-Tahini et al., 2005). Both rock skeleton and solid grain for an anisotropic poroelastic rock are a complex function of subjective stress, stiffness of each mineral, and pore stiffness. The pore stiffness again varies depending on isolated stiff pores and compliant ellipsoidal pores. We used the general singular approximation method for the static case to estimate the effective elastic properties from the rock composition and microstructure data. Any other effective medium scheme or mixing laws is also appropriate if calibrated properly with the experimental data. Our justifications for using the GSA method are explained in chapter 02. We modeled the compressional and shear wave velocities from mineral composition and porosity data of the Barnett Shale. The GSA method provided a good fit with the lab measured velocities of the Barnett Shale samples. However, the f parameter in the GSA method is more like a qualitative parameter. It should not be treated as a real connectivity property such as permeability or hydraulic conductivity. Moreover, fractures and porous inclusions are topologically isolated in the GSA method (Sayar and Torres-Verdin, 2016) in common derivations. We also demonstrated that the success of the GSA method specifically depends on the appropriate modeling scheme, which requires the rock physics understanding of the core samples.

We applied our theoretical equations from chapter three to the experimental data. We discussed in detail those applications in chapter four for different cases, such as changes in confining pressure, pore pressure, and uniaxial stress. We collected experimental data literature. However, experimental methods for measuring the Biot parameter and the governing equation for calculating the Biot parameter among different authors are also different. For example, the grain modulus (Kg) for Ma and Zoback (2017) data (in 4.2 - isotropic rock under pressure) is different at different confining pressure and pore pressure. Moreover, Kg increases up to approximately 325 GPa as pore pressure increases. Nevertheless, K^o (equivalent to Kg here) in the Biot tensor equation for the acoustic method of Scott and Abousleiman (2005) is taken as constant and independent of stress. Thus, calculated biot parameters from different types of experimental data may not give the exact same value.

Furthermore, there are always some uncertainties with compliance moduli (S^o - in our equation in chapter three) of solid grain for multimineral rocks as zero-porosity samples of such rocks are uncommon and rarely measured. Additional uncertainties in grain moduli may arise from how isolated pores are inaccessible to pore fluid or changes of pore connectivity with stress (Ma and Zoback, 2017). Theoretical assumptions of an equation may also become an issue depending on the rock's real behavior if different than the considered cases of elastic, non-linearly elastic, or anisotropic rock.

Our results for transversely isotropic rocks show significant differences between the vertical and horizontal components of the Biot tensor with stress and frequency in both experimental data and numerically modeled data for a TI media. We notice that applied stress and rock's intrinsic microstructure affect the Biot tensor conversely. Vertically applied uniaxial stress cause anisotropy to increase up to a stress point where maximum grain-to-grain contact is achieved, and open pores and compliant microcracks are effectively closed. We observe that α_{11} increases, but α_{33} decreases as uniaxial stress increases. The rock microstructure, on the other hand, especially the presence of aligned minerals, cause a decrease in α_{11}, but an increase in α_{33}.

Our proposed approach for medium under uniaxial stress shows an excellent prediction of α_{33} and α_{11} for a given stress. However, our method is only suitable when the stress magnitude is small compared to the elastic moduli of the media.

Apart from rock microstructure and stress, frequency also plays a vital role in the Biot tensor. Our numerical simulations based on the summation of the Dyson equation for the scattering effects of the inclusions show α_{11} and α_{33} have a peak value (at ~45 Hz) at the band of surface seismic frequency. Therefore, the proper method and data are necessary to ensure accurate estimation and practical application of the Biot coefficient. We didn't consider liquid viscosity in detail in our study. Future work on the evaluations of Biot tensor for time-lapse seismic applications should consider simultaneous variations of stress and frequency. Therefore, a robust method may also involve dynamic permeability and viscosity in the frequency domain while accounting for stress variations due to fluid injection or depletion.

Appendix A: Stiffness tensor of VTI media and coefficients of anisotropy for rocks with high magnitude of anisotropy

A transversely isotropic media with a vertical axis of symmetry (VTI) is the simplest anisotropic system. Five independent elastic constants can describe a VTI medium. The Voigt stiffness matrix for a VTI media has the form (Mavko et al., 2009):

$$C_{ij} = \begin{bmatrix} C_{11} & C_{12} & C_{13} & 0 & 0 & 0 \\ C_{12} & C_{11} & C_{13} & 0 & 0 & 0 \\ C_{13} & C_{13} & C_{33} & 0 & 0 & 0 \\ 0 & 0 & 0 & C_{44} & 0 & 0 \\ 0 & 0 & 0 & 0 & C_{44} & 0 \\ 0 & 0 & 0 & 0 & 0 & C_{66} \end{bmatrix}, C_{66} = 0.5(C_{11} - C_{12}) \quad \text{(A.1)}$$

And, the compliance tensor has the form:

$$S_{ij} = \begin{bmatrix} S_{11} & S_{12} & S_{13} & 0 & 0 & 0 \\ S_{12} & S_{11} & S_{13} & 0 & 0 & 0 \\ S_{13} & S_{13} & S_{33} & 0 & 0 & 0 \\ 0 & 0 & 0 & S_{44} & 0 & 0 \\ 0 & 0 & 0 & 0 & S_{44} & 0 \\ 0 & 0 & 0 & 0 & 0 & S_{66} \end{bmatrix}, S_{66} = 2(S_{11} - S_{12}) \quad \text{(A.2)}$$

Under the assumption of "weak" anisotropy, Thomsen (1986) suggested a convenient notation in terms of elastic constants for a VTI media.

Thomsen (1986) notations are given as (Mavko et al., 2009),

$$\begin{aligned} \varepsilon &= (C_{11} - C_{33}) / 2C_{33} \\ \gamma &= (C_{66} - C_{44}) / 2C_{44} \\ \delta &= (C_{13} + C_{44})^2 - (C_{33} - C_{44})^2 / 2C_{33}(C_{33} - C_{44}) \end{aligned} \tag{A.3}$$

Let us write the elastic constants in the above Equation in terms of velocities and density (ρ), we receive,

$$\begin{aligned} \varepsilon &= \frac{\rho V_p^2(90^o) - \rho V_p^2(0^o)}{2\rho V_p^2(0^o)} \\ &= \frac{V_p^2(90^o)}{2V_p^2(0^o)} - \frac{1}{2} \end{aligned} \tag{A.4}$$

And, similarly

$$\gamma = \frac{V_{sh}^2(90^o)}{2V_{sv}^2(0^o)} - \frac{1}{2} \tag{A.5}$$

Similar to the above notations, the coefficients of anisotropy which are valid for any magnitudes of anisotropy, are given below after Chesnokov (1977) as

$$\begin{aligned} \alpha_p &= \frac{V_p^2(90^o) - V_p^2(0^o)}{V_p^2(0^o)} \\ &= \frac{V_p^2(90^o)}{V_p^2(0^o)} - 1 \end{aligned} \tag{A.6}$$

and

$$\alpha_s = \frac{V_{SH}^2(90^o)}{V_{SV}^2(0^o)} - 1 \tag{A.7}$$

The above coefficients are appropriate for rocks like the Barnett Shale or any rocks with a high magnitude of anisotropy.

Appendix B: Derivation of the generalized singular approximation method (GSA)

We outline here a brief derivation of the GSA method. Let us consider two elastic bodies with equal size and shape, and they both have the same boundary conditions. One of them is a heterogeneous body with unknown effective stiffness C^*, and the other one is a homogeneous body with stiffness tensor C^c. Let's assume the displacement vectors are $u(x)$ and $u^c(x)$ in the inhomogeneous and homogeneous body for an applied force (F).

The equilibrium equations can be written as,

$$Lu = -F = L^c u^c \tag{B.1}$$

$$\textit{Where,}\ L_{ij} \equiv \nabla_j C_{ijkl} \nabla_k \ \textit{and}\ L_{il}^C \equiv \nabla_j C_{ijkl}^C \nabla_k)$$

We write all fields in the heterogeneous anisotropic body as a sum of the comparison body and fluctuations as below

$$\begin{aligned} u &= u^c + u' \\ C &= C^c + C' \\ L &= L^c + L' \end{aligned} \tag{B.2}$$

Where, u^c, C^c and L^c are the average value and u', $C'$and $L'$are the fluctuations

Using Equation (B.1) and Equation (B.2), we receive

$$L^c u' = -L' u \tag{B.3}$$

Let's introduce the Green tensor of the operator L^c in the form

$$L^c G = -I\delta(r) \tag{B.4}$$

Where I is the fourth-rank unit tensor and δ is the Dirac delta. We obtain a solution to the Equation (B.3) as

$$u' = G * L'u \tag{B.5}$$

Where sign '∗' means convolution. Then, utilizing Equation (B.5), we get a relation between the local and average strain similar to the Lippman–Schwinger equation of the quantum scattering theory

$$\varepsilon_{ij}(x) = \varepsilon_{ij}^c(x) + \int G_{k(i,j)l}(x - x_1)[C_{klmn}(x_1) - C_{klmn}^c]\varepsilon_{mn}(x_1)dx_1 \tag{B.6}$$

Where $G_{ki,jl}$ are the components of the second derivative of Green's function of the comparison body. The second derivative of Green's function is a generalized function, and it can be presented as a sum of the singular part and formal part. For randomly distributed inclusions, the singular part is much larger than the formal part. It has been verified by comparing with the experimental data (Bayuk and Chesnokov, 1998). Therefore, only the singular part is considered in the GSA method, and the formal part is omitted. Symmetrization is performed over the indices in the parentheses in the Equation (B.6). The second derivative of the Green's function in Equation (B.6) is also symmetrized over the outer pair of indices (k and l) and replaced by its only singular part 'g' as given below:

$$g_{kmln} = -\frac{1}{4}(\tilde{a}_{klnm} + \tilde{a}_{mlnk} + \tilde{a}_{knlm} + \tilde{a}_{nmlk})$$

$$\tilde{a}_{kmln} \equiv \frac{1}{4}\int_0^{2\pi}\int_0^{\pi} n_{mn}\Lambda_{kl}^{-1} d\Omega, \text{where } d\Omega \equiv \sin\theta d\theta d\varphi \tag{B.7}$$

$$\Lambda_{kl} \equiv C_{kmln}^{C} n_{mn},\ n_{mn} \equiv n_m n_n$$

$$n_1 = \frac{1}{a_1}\sin\theta\cos\varphi,\quad n_2 = \frac{1}{a_2}\sin\theta\sin\varphi,\quad n_3 = \frac{1}{a_3}\cos\theta$$

Where a_1, a_2, and a_3 are the semi-axes of the ellipsoidal heterogeneities. It is assumed that all heterogeneities are of ellipsoidal shape in the GSA derivation. After the second derivative of Green's function is found, the Equation (B.6) can be written as

$$\varepsilon_{ij}(x) = \varepsilon_{ij}^{c}(x) + g_{ijkl}[C_{klmn}(x) - C_{klmn}^{c}]\varepsilon_{mn}(x) \tag{B.8}$$

Performing index permutation, we obtain

$$\varepsilon_{ij}(x) = I_{ijmn}\varepsilon_{mn}(x) \tag{B.9}$$

and then Equation (B.8) can be rewritten in the form

$$\varepsilon_{mn}(x) = \{I_{mnij} - g_{mnkl}[C_{klij}(x) - C_{klij}^{c}]\}^{-1}\varepsilon_{ij}^{c} \tag{B.10}$$

Multiplying both the sides of Equation (B.10) by the stiffness tensor and averaging them over representative volume element (RVE) we obtain

$$\langle C(x)\varepsilon(x)\rangle = \langle C(x)\{I - g[C(x) - C^{c}]\}^{-1}\varepsilon^{c} \tag{B.11}$$

The average strain for the comparison body can also be obtained from Equation (B.10)

$$\varepsilon^c = \langle I - g[C(x) - C^c]\}^{-1}\rangle^{-1}\langle\varepsilon(x)\rangle \tag{B.12}$$

The effective elastic tensor relates the average stress of the media to the average strain and therefore

$$\langle\sigma(x)\rangle = C^*\langle\varepsilon(x)\rangle \tag{B.13}$$

Therefore, we obtain the formula for the effective stiffness of the inhomogeneous body utilizing Equation (B.11) and Equation (B.12).

$$C^* = \langle C(x)[I - g(C(x) - C^c)]^{-1}\rangle^{-1}\langle[I - g(C(x) - C^c)]^{-1}\rangle^{-1} \tag{B.14}$$

Note that a similar equation is also available from Willis (1977). However, his method of derivation is different from Shermergor (1977).

Bibliography

Ahrens, T. J., Johnson, M. L., 1995, Mineral Physics & Crystallography: A Handbook of Physical Constants, Washington, DC, USA, Wiley Online Library, AGU reference shelf.

Alkhimenkov, Y., and Bayuk, I. O., 2017, Unified Effective Medium Theory for Cracked Porous Rocks - Theory and Case Study, in Proceedings 79th EAGE Conference and Exhibition, Paris, France, 2017, European Association of Geoscientists & Engineers, p. 1 - 5.

Al-Tahini, A. M., Abousleiman, Y. N., and L. Brumley, J. L., 2005, Acoustic and Quasistatic Laboratory Measurement and Calibration of the Pore Pressure Prediction Coefficient in the Poroelastic Theory: SPE Annual Technical Conference and Exhibition: Dallas, USA, Society of Petroleum Engineers, p. 1-8.

Bayuk, I., and Chesnokov, E., 1998, Correlation between elastic and transport properties of porous cracked anisotropic media: J. Phys. Chem. Earth., v. 23, no. 3, p. 361–366.

Bayuk, I. O., Ammerman, M., and Chesnokov, E.M., 2007, Elastic moduli of anisotropic clay: Geophysics, v. 72, no. 5, p. D107-D117.

Berryman, J. G., 1992, Single-scattering approximations for coefficients in Biot's equations of poroelasticity: .J. Acoust. Soc. Am., v. 91, p. 551–571.

Biot, M. A., 1956, Theory of propagation of elastic waves in a fluid saturated porous solid. I. Low frequency range and II. Higher-frequency range: J. Acoust. Soc. Am., v. 28, p. 168–191.

Biot, M. A., and Willis, D. G., 1957, The elastic coefficients of the theory of consolidation: Journal of Applied Mechanics, v. 79, p. 594–601.

Biot, M. A., 1962, Mechanics of deformation and acoustic propagation in porous media: J. Appl. Phys., v. 33, p. 1482–1498.

Bland, D. R., 1969, Nonlinear dynamic elasticity, Waltham, MA, USA, Blaisdell publishing, 93p.

Carroll, M. M., 1979, An effective stress law for anisotropic elastic deformation: Journal of Geophysical Research, v. 84, p. 7510–7512.

Cheng, A. H. D., 1997, Material coefficients of anisotropic poroelasticity: International Journal of Rock Mechanics and Mining Sciences, v. 34, p. 199–205.

Chesnokov, E. M., 1977, Seismic anisotropy of the Earth's Upper Mantle, Moscow, Nauka (in Russian), 144 p.

Chesnokov, E., Morshed, S., and Vikhoreva, A., 2019, Biot-Willis parameter in a poroelastic anisotropic media saturated with low viscosity liquid, static and dynamic case: 81st EAGE Conference and Exhibition: London, UK, European Association of Geoscientists & Engineers, p. 1–5.

Chesnokov, E. M., Kukharenko, Y. A., and Kukharenko, P. A., 1995, Method of diagram technique for calculation of effective physical parameters of microinhomogeneous media: SPIE: International Society of Optical Engineers, Mathematical Methods in Geophysical Imaging, v. III, p. 2571, 2572–2512.

Chesnokov, E. M., Bell, D. W., Kukharenko, Y. A., and Chourayev, A. N., Effective stress influence on elastic constants of fluid filled porous media: Proceedings Second Biot Conference on Poromechanics, Grenoble, France, 2002, Volume Poromechanics II, p. 879–882.

Chesnokov, E. M., Ammerman, M., Sinha, S., and Kukharenko, Y. A., 2005, Tensor character of Biot parameter in poroelastic anisotropic media under stress: static and dynamic cases, Rainbow in the earth, 2nd international workshop

Chesnokov, E. M., Tiwary, D. K., Bayuk, I. O., Sparkman, M. A., and Brown, R. L., 2009, Mathematical modelling of anisotropy of illite-rich shale: Geophysical Journal International, v. 178, no. 3, p. 1625-1648.

Dahlen, F. A., 1972, Elastic velocity anisotropy in the presence of an anisotropic initial stress: Bulletin of the Seismological Society of America, v. 62, p. 1183–1193.

Eshelby, J. D., 1957, The determination of the elastic field of an ellipsoidal inclusion, and related problems: Proceedings of the Royal Society of London. Series A. Mathematical and Physical Sciences, v. 241, no. 1226, p. 376-396.

Gebrande, H., 2005, 3.1.3 Elastic wave velocities and constants of elasticity of rocks at room temperature and pressures < 1 GPa, Landolt-Börnstein - Group V Geophysics, Volume 1B, Springer-Verlag Berlin Heidelberg.

Ghosh, A., and Morshed, S., 2021, A Green's function approach to the study of effective anisotropic properties of the Barnett Shale: Geophysical Prospecting, (published online https://doi.org/10.1111/1365-2478.13082), v. (paper version is in press).

Gurevich, B., 2004, A simple derivation of the effective stress coefficient for seismic velocities in porous rocks: Geophysics, v. 69, p. 393–397.

Hashin, Z., and Shtrikman, S., 1963, A variational approach to the elastic behavior of multiphase materials: J. Mech. Phys. Solids, v. 11, no. 2, p. 127–140.

Herwanger, J., and Koutsabeloulis, N., 2011, Seismic geomechanics: how to build and calibrate geomechanical models using 3D and 4D seismic data, Houten, The Netherlands, European Association of Geoscientists and Engineers.

Hill, R., 1965, A self-consistent mechanics of composite materials: J. Mech. Phys. Solids, v. 11, p. 357–372.

Hudson, J. A., 1980, Overall properties of a cracked solid Math. Proc. Camb. Phil. Soc., v. 88, p. 371–384.

Jakobsen, M., Hudson, J.A., and Johansen, T.A., 2003, T-matrix approach to shale acoustics: Geophys. J. Int., v. 154, no. 2, p. 533–558.

Jarvie, D. M., Hill, R. J., Ruble, T. E., and Pollastro, R. M., 2007, Unconventional shale-gas systems: The Mississippian Barnett Shale of north-central Texas as one model for thermogenic shale-gas assessment: AAPG Bulletin, v. 91, no. 4 p. 475–499.

Jiang, T., 2013, Connection of elastic and transport properties: Effective medium study in anisotropic porous media: PhD dissertation: University of Houston.

Liao, Q., 2012, Wavelet Approaches to Seismic Data Analysis: PhD dissertation: University of Houston.

Loucks, R. G., and Ruppel, S. C., 2007, Mississippian Barnett Shale: Lithofacies and depositional setting of a deep-water shale-gas succession in the Fort Worth Basin, Texas: AAPG Bulletin, v. 91, no. 4, p. 579-601.

Loucks, R. G., Reed, R. M., Ruppel, S. C., and Hammes, U., 2012, Spectrum of pore types and networks in mudrocks and a descriptive classification for matrix-related mudrock pores: AAPG Bulletin, v. 96, no. 6, p. 1071-1098.

Loucks, R. G., Reed, R. M., Ruppel, S. C., and Jarvie, D. M., 2009, Morphology, Genesis, and Distribution of Nanometer-Scale Pores in Siliceous Mudstones of the Mississippian Barnett Shale: Journal of Sedimentary Research, v. 79, no. 12, p. 848-861.

Lu, K., 2016, Gas shale anisotropy and mechanical property: laboratory measurements and mathematical modeling: PhD dissertation: University of Houston.

Ma, X., and Zoback M. D., 2017, Laboratory experiments simulating poroelastic stress changes associated with depletion and injection in low-porosity sedimentary rocks: Journal of Geophysical Research: Solid Earth, v. 122.

Mavko, G., Mukerji, T. , and Dvorkin, J., 2009, The rock physics handbook, tools for seismic analysis of porous media, Cambridge, UK, Cambridge University Press.

Metwally, Y. M., and Chesnokov, E.M., 2012, Clay mineral transformation as a major source for authigenic quartz in thermo-mature gas shale: Applied Clay Science, v. 55, p. 138–150.

Mori, T., and Tanaka K., 1973, Average stress in matrix and average elastic energy of materials with misfitting inclusions: Acta Metall, v. 21, p. 571–574.

Morshed, S. M., Chesnokov, E. M., and Vikhoreva, A. A., 2021, Biot effective stress parameter in poroelastic anisotropic media: Static and dynamic case: Geophysical Prospecting, v. 69, no. 3, p. 530-541.

Müller, T. M., and Sahay, P.N. , 2016, Generalized poroelasticity framework for micro-inhomogeneous rocks: Geophysical Prospecting, 64, 1122–1134., v. 64, p. 1122–1134.

Nikitin, L. V., and Chesnokov, E.M., 1981, The influence of stress condition on the anisotropy of elastic properties in a medium: Izvestiya, Physics of the Solid Earth (English translation), v. 17, no. 3, p. 174–183.

Nikitin, L. V., and Chesnokov, E.M., 1984, Wave propagation in elastic media with stress-induced anisotropy: Geophysical Journal of the Royal Astronomical Society, v. 76, p. 129–133.

Nishizawa, O., 1982, Seismic velocity anisotropy in a medium containing oriented cracks - transversely isotropic case: Journal of Physics of the Earth, v. 30, p. 331-347.

Nur, A., and Simmons, G., 1969, Stress-induced velocity anisotropy in rocks: an experimental study: J. Geophys. Res., v. 74, p. 6667-6674.

Nur, A., and Byerlee, J.D. , 1971, An exact effective stress law for elastic deformation of rocks with fluids: J. Geophys. Res., v. 76, p. 6414–6419.

Pollastro, R. M., Jarvie, D. M., Hill, R. J., and Adams, C. W., 2007, Geologic framework of the Mississippian Barnett Shale, Barnett-Paleozoic total petroleum system, Bend arch–FortWorth Basin, Texas: AAPG Bulletin, v. 91, no. 4, p. 405–436.

Quinones, L., DeShon, H. R., Jeong, S., Ogwari, P., Sufri, O., Holt, M. M., and Kwong K. B., 2019, Tracking Induced Seismicity in the Fort Worth Basin: A Summary of the 2008–2018 North Texas Earthquake Study Catalog: Bulletin of the Seismological Society of America, v. 109, no. 4, p. 1203–1216.

Rasolofosaon, P., 1998, Stress-induced seismic anisotropy revisited: Revue de l'Institut Francais du Petrole, v. 53, p. 679–692.

Raymer, D. G., Tommasi, A., and Kendall, J. M., 2000, Predicting the seismic implications of salt anisotropy using numerical simulations of halite deformation: Geophysics, v. 65, p. 1272–1280.

Rytov, S. M., Kravtsov,Y. A., and Tatarskii, V. I., 1989, Principles of statistical radiophysics 4, Berlin Heidelberg, Springer-Verlag, Wave Propagation Through Random Media.

Sanchez-Valle, C., Ghosh, S., and Rosa, A. D., 2011, Sound velocities of ferromagnesian carbonates and the seismic detection of carbonates in eclogites and the mantle.: Geophysical Research Letters, v. 38.

Sayar, P., and Torres-Verdín, C., 2016, Using anisotropic effective medium theories to quantify elastic properties of sandstone-shale laminated rocks: Geophysics, v. 81, no. 4, p. D315–D333.

Sayers, C. M., 2010, Geophysics Under Stress: Geomechanical Applications of Seismic and Borehole Acoustic Waves Tulsa, OK, USA, Society of Exploration Geophysicists and European Association of Geoscientists and Engineers, Distinguished Instructor Series.

Scott, E. T., and Abousleiman, Y., 2005, Acoustic measurements of the anisotropy of dynamic elastic and poromechanics moduli under three stress/strain pathways: Journal of Engineering Mechanics, v. 131, no. 9, p. 937–946.

Sevostianov, I., and Giraud, A., 2013, Generalization of Maxwell homogenization scheme for elastic material containing inhomogeneities of diverse shape: Int. J. Eng. Sci., v. 64, p. 23-36.

Shermergor, T. D., 1977, Theory of elasticity of microinhomogeneous media, Moscow, Nauka (in Russian).

Siggins, A. F., and Dewhurst, D.N., 2003, Saturation, pore pressure and effective stress from sandstone acoustic properties: Geophysical Research Letters, v. 30, no. 2, p. 1089.

Siggins, A. F., Dewhurst, D.N., and Dodds, K. , 2004, Effective stress and the Biot-Willis coefficient for reservoir sandstones, SEG Annual Meeting, Volume 23: Denver, USA, Society of Exploration Geophysicists p. 1770–1773.

Skempton, A. W., 1954, The pore pressure coefficients A and B: Geotechnique, p. 143–147.

Sone, H., and Zoback, M.D., 2013, Mechanical properties of shalegas reservoir rocks - Part 1: Static and dynamic elastic properties and anisotropy: Geophysics, v. 78, no. 5, p. D381–D392.

Sviridov, V. A., Mayr, S. I., and Shapiro, S. A., 2017, Elastic properties of two VTI shale samples as a function of uniaxial stress: experimental results and application of the porosity-deformation approach, Geophysics, v. 82, no. 6, p. C201–C210.

Terzaghi, K., 1923, Die Berechnung der Durchlassigkeitsziffer des Tones aus dem Verlauf der hydrodynamischen Spannungserscheinungen, Akademie der Wissenschaften in Wien, Sitzungsberichte, Mathematisch-naturwissenschaftliche Klasse, v. 132, p. 125–138.

Thompson, M., and Willis, J. R., 1991, A reformulation of the equations of anisotropic poroelasticity: Journal of Applied Mechanics ASME, v. 58, p. 612–616.

Thomsen, L., 1986, Weak elastic anisotropy: Geophysics, v. 51, p. 1954-1966.

Thurston, R. N., and Brugger, K., 1964, Third-order elastic constants and the velocity of small amplitude elastic waves in homogeneously stressed media: Physical Review, v. 133, no. 6A, p. A1604–A1610.

Thurston, R. N., 1965, Effective elastic coefficients for wave propagation in crystals under stress Journal of the Acoustical Society of America, v. 37, no. 2, p. 348–356.

Todd, T., and Simmons, G., 1972, Effect of pore pressure on the velocity of compressional waves in low porosity rocks: J. Geophys. Res., v. 77, p. 3731–3743.

Vikhorev, A. A., and Chesnokov, E. M., 2009, Effective dynamic properties of randomly inhomogeneous medium defined by statistically homogeneous correlation functions, SEG Annual meeting: Houston, USA, p. 917–923.

Wang, Z., 2002, Seismic anisotropy in sedimentary rocks, part 1: A single-plug laboratory method: Geophysics, v. 67, no. 5, p. 1415-1422.

Willis, J., 1977, Bounds and self-consistent estimates for the overall properties of anisotropic composites: J. Mech. Phys. Solids, v. 25, p. 185–202.

Zhou, X., and Ghassemi, A.M., 2019, Biot's effective stress coefficient tensor measurements on Mancos shale, 53rd US Rock mechanics/geomechanics symposium: New York, NY, USA, p. 19–516.

Zimmerman, R. W., 1991, Compressibility of Sandstones, Amsterdam, The Netherlands, Elsevier Science, Developments in Petroleum Science.